JOC The Journal of Organic Chemistry

Article

Bulk Inclusions of Double Pyridazine Molecular Rotors in Hexagonal Tris(*o*-phenylene)cyclotriphosphazene (TPP)

Ji#í Kaleta, Guillaume Bastien, Jin Wen, Martin Dracinsky, Edward Tortorici, Ivana Cisarova, Paul D. Beale, Charles T. Rogers, and Josef Michl

J. Org. Chem., **Just Accepted Manuscript** • DOI: 10.1021/acs.joc.9b00553 • Publication Date (Web): 27 May 2019

Just Accepted

is published by the American Chemical Society. 1155 Sixteenth Street N.W., Washington, DC 20036

Bulk Inclusions of Double Pyridazine Molecular Rotors in Hexagonal Tris(*o*-phenylene)cyclotriphosphazene (TPP)

Jiří Kaleta,[a,b]* Guillaume Bastien,[a] Jin Wen,[a]* Martin Dračínský,[a] Edward Tortorici,[c] Ivana Císařová,[d] Paul D. Beale,[c] Charles T. Rogers,[c] and Josef Michl[a,b]

[a] *Institute of Organic Chemistry and Biochemistry AS CR, Flemingovo nám. 2, 166 10 Prague 6, Czech Republic.*
[b] *Department of Chemistry, University of Colorado, Boulder, CO 80309-0215, United States*
[c] *Department of Physics, University of Colorado, Boulder, CO 80309, United States*
[d] *Department of Inorganic Chemistry, Faculty of Science, Charles University in Prague, Hlavova 2030, 12840 Prague 2, Czech Republic.*

TOC Graphic

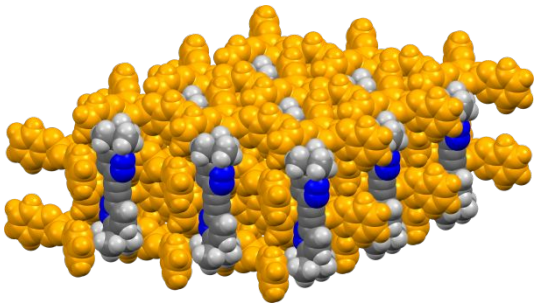

ABSTRACT

A new generation of double pyridazine molecular rotors differing in intramolecular dipole-dipole spacing was synthesized. All rotor molecules formed bulk inclusions in tris(*o*-phenylenedioxy)cyclotriphosphazene (TPP) host. Results of dielectric spectroscopy were fitted to a pair of nine-state models that accounted for interactions of neighboring dipoles at the either aligned or opposed possible orientation of the local three-fold dipole rotation potentials within a channel of the TPP host. The results indicate dipole-dipole interaction strengths at the 100 to 200 K scale that lead dipoles to preferentially populate a subset of low-energy configurations. They also reveal that pyridazines with ethynyl substituents in positions 3- and 6- have slightly higher rotational barriers (3.2 - 3.5 kcal/mol) than those carrying one ethynyl and one *tert.*-Bu group (1.9 - 3.0 kcal/mol). Upon cooling, these barriers reduce the rate of thermal transitions between the potential wells so much that the inclusions cannot achieve ordered dipolar ground states.

INTRODUCTION

Preparation and study of regular two- and three-dimensional (2D and 3D) assemblies of molecular level devices are attracting considerable attention as documented by many original articles, reviews and book chapters published in recent years.[1,2,3,4,5,6,7] In general, 2D arrays of molecular devices are accessible using the Langmuir-Blodgett technique,[8,9,10] self-assembly on suitable (mostly metallic) substrates,[11,12,13,14,15,16] or formation of surface inclusions by host-guest interaction,[17,18,19] where anchoring parts of molecular devices are inserted inside pores in the host lattice, while their functional parts protrude outside the surface. The 3D materials are usually made by (co-)crystallization of individual components[20,21,22,23,24,25,26] or by sorption of guest molecules into a well organized porous

host matrix, such as a MOF[27,28,29] or hexagonal tris(*o*-phenylene)cyclotriphosphazene (TPP, Figure 1).[30,31]

We report results obtained with 3D assemblies of dipolar molecular rotors **1** - **5** (Chart 1) present as guests in the channels of TPP. The crystal structure of this host is composed of ~5 Å thick layers, with the neighboring layers rotated by 60°. The layers contain voids that are superimposed to form channels oriented perpendicular to the layers and located ~11 Å apart in a triangular arrangement. Although in each layer, the channel cross-section is triangular, the staggering of the layers makes them appear hexagonal when viewed along their axes.[31] The internal diameter is 4.5 - 5 Å. Since the crystal is molecular, this diameter and the channel-to-channel spacing are capable of expanding by as much as 10% when the channels are filled with guest molecules.[6,28]

Our motivation is the desire to improve our understanding of dipole-dipole interactions in these regular arrays and especially, of the effect of the locally trigonal structure of the channels. The lateral distances between two neighboring dipoles are fixed by the inter-channel distance and can be modified only slightly. However, the rotors **1** - **5** offer a variety of intra-channel distances between neighbors, and we can investigate both those situations in which neighboring dipoles are located in congruent triangular environments and those in which their environments are mutually rotated by 60°. An understanding of dipole-dipole interactions plays a key role in the design of potential collective behavior. Ferroelectric phases[32] would be particularly interesting since they are promising potential applications in the field of (nano)electronics (memory devices, frequency filters, etc.).

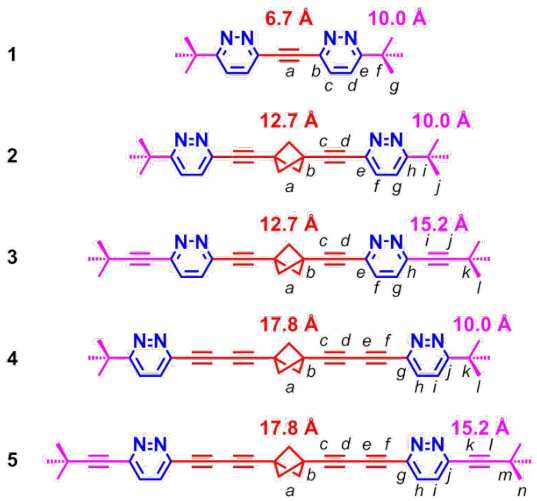

Chart 1. Structures of Double Pyridazine Rotors **1** - **5** with Intramolecular (red) and Intermolecular (purple) Pyridazine - Pyridazine Center to Center Distances Shown. Intermolecular distances are calculated for two neighboring molecules located next to each other within one TPP channel. Black italic letters indicate the labeling of carbon atoms used in Table S3.

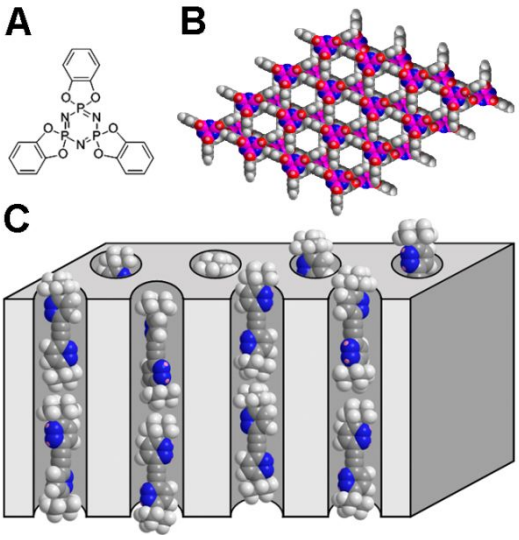

Figure 1. Chemical formula of TPP (A), top view of two successive layers of TPP (B), and a idealized model of molecular rotors anchored inside the TPP host (C).

The five rod-like molecular rotors **1** - **5** have four structural features in common: (i) a bulky terminal *tert.*-butyl group, whose diameter exceeds that of a rotating pyridazine ring, and which expands the interior of the TPP channel and thus reduces the barrier for dipole rotation; (ii) two pyridazine rotators with a relatively small diameter (~5.80 Å) and high dipole moment (4.1 Debye for pyridazine itself[33]); (iii) a bulky bicyclo[1.1.1]penta-1,3-diyl group (except in **1**) with diameter of ~6.30 Å, which holds the axle of the rotor molecule centered in the channel, away from the channel walls, limiting possible wobbling motions,[27] and also serves as a ^{13}C NMR marker since its chemical shifts occur in an uncluttered spectral region; (iv) a well-defined intramolecular pyridazine-pyridazine center to center distance. Intermolecular rotator-rotator distances depend on guest loading. For saturated samples no voids between rotor molecules within a channel are expected, and these distances will be the sum of the lengths of terminal groups (Chart 1). If the strength of dipole-dipole interactions is sufficient and the barriers are low enough, compounds with both inter- and intramolecular dipole-dipole spacings within a channel smaller than inter-channel separation (**1** - **4**) would yield an antiferroelectric phase, while **5** would produce a ferroelectric phase.

The pyridazine rotator also suffers from a drawback. Since the C-N and N-N bonds are shorter (1.32 - 1.34 Å) than the remaining aromatic C-C bonds (1.37 - 1.40 Å), the exocyclic C-C bonds in positions 3- and 6- are not exactly antiparallel (an averaged deviation is ca 4°), giving the rotor molecule a banana shape. Such bending may increase rotational barriers.

RESULTS

We describe the synthesis of double pyridazine molecular rotors **1** □ **5**, demonstrate their ability to form bulk inclusions in TPP, and prove that all parts of the molecule and especially the pyridazine units rotate inside TPP crystals. The inclusions were characterized by ^{13}C and ^{31}P cross-polarization magic angle spinning (CP-MAS) and ^{31}P single-pulse excitation (SPE) solid-state NMR, powder X-ray diffraction (XRD), differential scanning calorimetry (DSC), and dielectric spectroscopy. Pyridazine rotational barriers were

determined by dielectric spectroscopy and for **5** the lower limit of rotational rate was also independently deduced from ssNMR. The results were accounted for by a nine-state model that takes into account dipole-dipole interactions and is supported by MP6-D3H4[34] and B97-D3/SVP[35] calculations. The structures of six of the new compounds were confirmed by single-crystal X-ray diffraction.

Synthesis. The shortest rotor **1** was synthesized in seven steps from 3,3-dimethylbutanone (Scheme 1), whose condensation with glyoxylic acid monohydrate followed by workup with aqueous ammonia provided the ammonium salt of 3-pivaloyllactic acid (**6**)[36] in the first step. Subsequent cyclization with hydrazine yielded the pyridazinone **7**,[36] which was aromatized and converted to the chloropyridazine **8** using $POCl_3$. The reactivity of the pyridazine ring was enhanced by substitution of the chlorine atom by iodine using aromatic Finkelstein reaction, which provided **9** in nearly quantitative yield. Subsequent Sonogashira coupling with TMSA afforded the silyl derivative **10**, which was treated with TBAF in THF to liberate the alkyne **11**. Final Sonogashira coupling between **11** and **9** afforded the rotor **1** in 90% yield (Scheme 1).

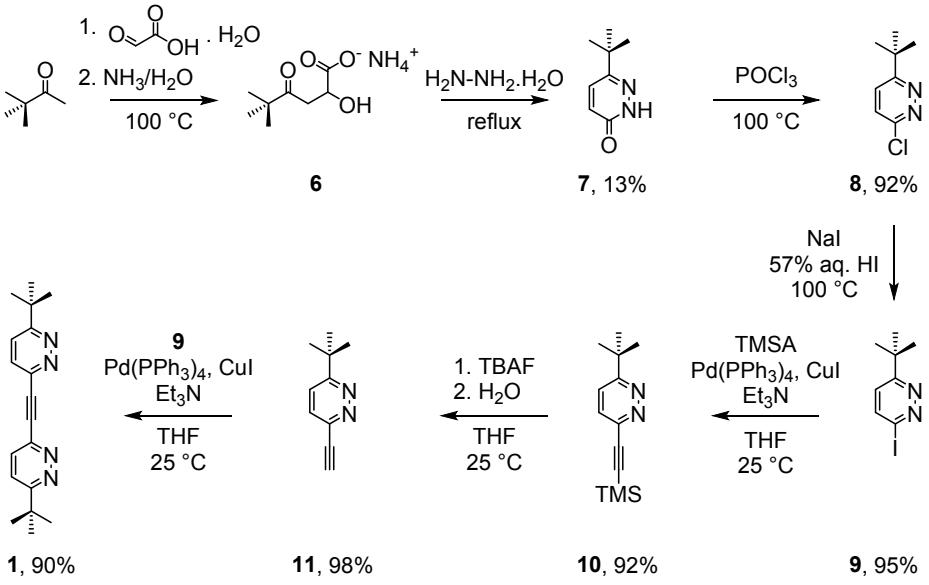

Scheme 1. Synthesis of Rotor **1**.

The extended pyridazine derivative **12** was made in two steps from 3,6-dichloropyridazine (**13**, Scheme 2). Reaction of cheap and commercially available **13** with NaI in concentrated aqueous HI afforded the much more expensive 3,6-diiodopyridazine (**14**) in excellent yield. Subsequent desymmetrization using Sonogashira coupling with 3,3-dimethylbut-1-yne gave a mixture of pyridazines **12** and **15**,[28] easily separated by column chromatography.

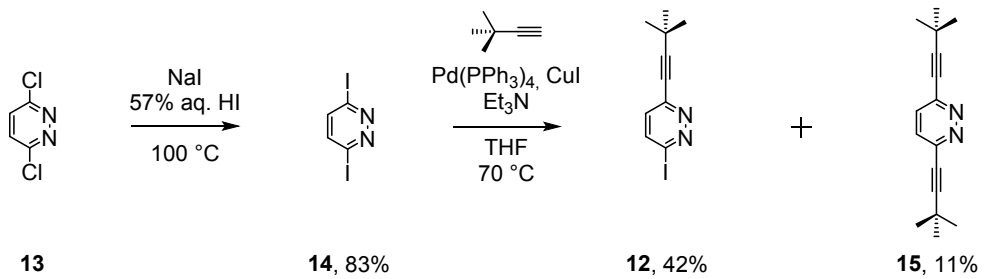

Scheme 2. Preparation of Asymmetric Pyridazine **12**.

Molecular rotors **2** and **3** were made in one-pot two-step syntheses from the bissilyl derivative **16**[37,38] (Scheme 3). Addition of TBAF in THF caused immediate cleavage of both TMS groups, and the free diyne **17** underwent Sonogashira coupling either with **9** to give **2** in 82% yield, or with **12** to provide **3** in 73% yield.

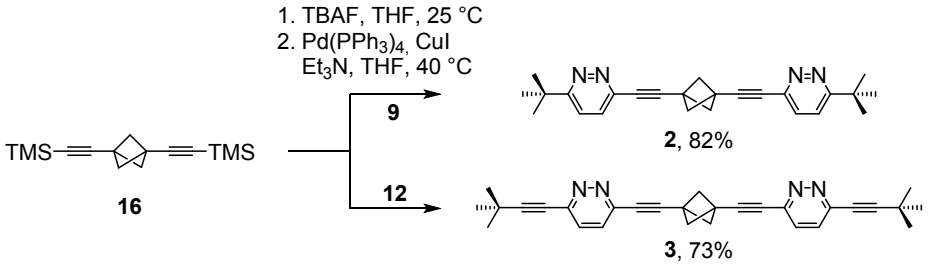

Scheme 3. Synthesis of Rotors **2** and **3**.

The next focus was the synthesis of the tetrayne **18** from the diyne **17**[37] (Scheme 4). Stepwise construction of two additional triple bonds started with double lithiation of **17**[37] followed by reaction with solid paraformaldehyde, which resulted in the diol **19**. Dess-Martin periodinane oxidized **19** to the dialdehyde **20** (with a distinctive mushroom-like odor), whose reaction with CBr_4 in presence of PPh_3 gave the tetrabromo derivative **21** in high yield. Final dehydrobromination with *n*-BuLi in ether provided the volatile and highly explosive tetrayne **18** as white crystalline solid with a characteristic acetylene-like odor (Scheme 4).

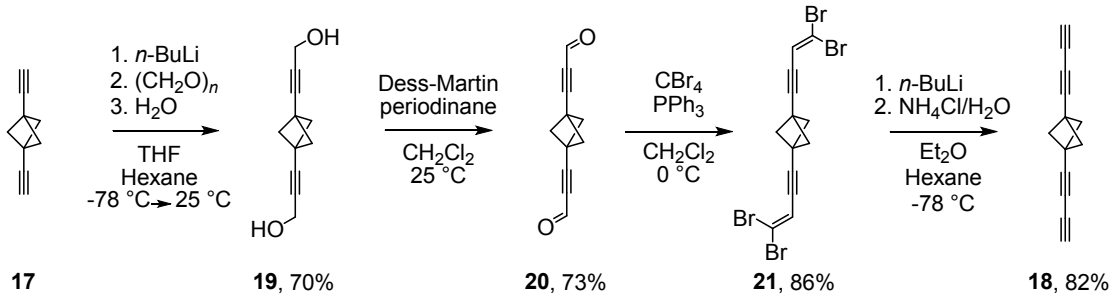

Scheme 4. Construction of Tetrayne **18**.

Finally, long molecular rotors **4** and **5** were prepared from tetrayne **18** and iodo derivatives **9** or **12** using standard Sonogashira coupling (Scheme 5). Both compounds were obtained as white crystalline solids, which detonate at temperatures above 200 °C.

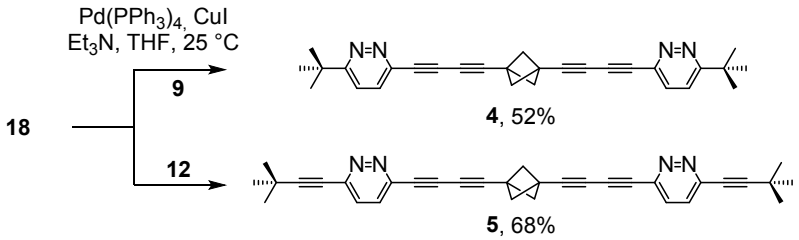

Scheme 5. Assembly of Rotors **4** and **5**.

Crystallography. Single crystals suitable for X-ray diffraction were obtained for two molecular rotors (**1** and **2**) and four intermediates, **9**, **18**, **19**, and **21**. The basic crystallographic parameters are summarized in Table S1 (Supporting Information).

Rotors **1** and **2** crystallized readily from CH_2Cl_2 solutions. In contrast, all attempts to obtain suitable single crystals of the other three rotors **3** - **5** failed. This is in agreement with previous observations where linear rigid 1,3-diethynylbicyclo[1.1.1]pentane (**17**) derivatives longer than ~19 Å usually provided microcrystalline material, not suitable for standard X-ray diffraction.

The highly explosive hydrocarbon **18** crystallized from CH_2Cl_2 solution in form of colorless short thick needles which turned brown/black after less than one hour. Low stability of these crystals significantly complicated their X-ray analysis and final structure suffers from a relatively high R factor of 9.31.

Compounds **1**, **2**, **19**, and **21** crystallized in monoclinic crystal system and P $2_1/n$, C 2/c, P $2_1/n$, and P $2_1/c$ space groups, respectively. Compound **9** formed orthorhombic crystals with P $2_12_12_1$ space group, while **18** crystallized in tetragonal crystal system and the P 4_2bc space group.

Selected interatomic distances for bicyclo[1.1.1]pentane (BCP) derivatives are summarized in Table 1 (Figure 2). The length of bond α is dictated by the substituent R and varies from 1.378 to 1.466 Å. As expected, the conjugated bonds in **2**, **18**, and **21** are shorter (1.378 - 1.441 Å) than the one adjacent to the CH_2OH group in **19** (1.466 Å). Interatomic distances β, γ, and δ are almost constant and comparable to those in previously published structures.[38] The length of triple bond β varies from 1.194 to 1.198 Å. The length of the exocyclic bridgehead C-C bond γ is 1.438 - 1.446 Å, and the inter-bridgehead distance δ lies between 1.881 and 1.888 Å.

Table 1. Selected Interatomic Distances in BCP Derivatives **2**, **18**, **19**, and **21**.

Cmpd.	R	Selected Interatomic Distances (Å)			
		α	β	γ	δ
2	6-*t*Bu-pyridazin-3-yl	1.441	1.195	1.446	1.884
18	CCH	1.378	1.198	1.438	1.881
19	CH_2OH	1.466	1.194	1.446	1.886
21	$CHCBr_2$	1.419	1.194	1.445	1.888

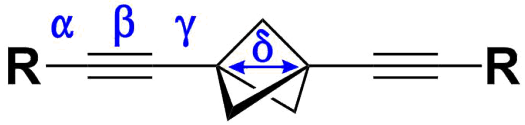

Figure 2. Labels of interatomic distances used in Table 1.

Preparation and Characterization of Bulk Inclusions. Bulk inclusion compounds are referred to as X%Y@TPP-d_{12}, where X represents the molar percentage of rotor Y (**1** - **5**). They were prepared by ball-milling neat guests **1** - **5** with freshly synthesized and solvent-free hexagonal TPP-d_{12} and subsequent annealing at 70 °C for 24 h. Each guest compound was used for the synthesis of two bulk inclusions differing in guest concentration (Table 2): unsaturated (incompletely guest-loaded) and saturated (TPP channels are full and the surplus of guest is located outside). Maximum guest loading was estimated as described in

Supporting Information, page S2. It depends on the length of the guest molecules and is ~30 mol% for the shortest rotor **1** (16.7 Å), and only ~15 mol% for the longest one (**5**, 33.0 Å).

Table 2. Bulk Inclusion Compounds Prepared.

Cmpd.	Guest Length (Å)	Estimated Maximum Guest Loading (molar%)	Sample Name[a]
1	16.7	31	30%**1**@TPP-d_{12} (unsaturated)
			40%**1**@TPP-d_{12} (saturated)
2	22.7	22	15%**2**@TPP-d_{12} (unsaturated)
			30%**2**@TPP-d_{12} (saturated)
3	27.9	18	20%**3**@TPP-d_{12} (unsaturated)
			25%**3**@TPP-d_{12} (saturated)
4	27.8	18	15%**4**@TPP-d_{12} (unsaturated)
			30%**4**@TPP-d_{12} (saturated)
5	33.0	15	15%**5**@TPP-d_{12} (unsaturated)
			25%**5**@TPP-d_{12} (saturated)

[a] Degree of saturation was confirmed by ^{13}C solid-state NMR.

Solid-state NMR was used to (i) characterize the bulk inclusions, (ii) study cross-polarization dynamics to understand spectral irregularities, and (iii) demonstrate that all parts of the rotor molecule rotate inside the channel and determine the lower limit to rotation rate in (15%**5**@TPP-d_{12}).

(i) Characterization of Bulk Inclusions. The NMR behavior of all inclusion compounds was studied by ^{13}C cross-polarization magic-angle spinning (CP MAS), ^{31}P CP MAS, and ^{31}P single pulse excitation (SPE). In Table S3 (Supporting Information), solid-state ^{13}C NMR chemical shifts of neat rotors **1** - **5** and their unsaturated inclusions in TPP are compared with chemical shifts of the rotors in $CDCl_3$ solution, using atom labels shown in Chart 1.

In general, solid-state NMR spectra of neat **1** - **5** resemble their solution ^{13}C NMR spectra, but some signals are slightly upfield or downfield shifted. The only exception is compound **2** whose signals in ^{13}C solid-state NMR spectrum are doubled due to presence of two inequivalent shielding environments within the unit cell.

Spectra of all inclusion compounds contain three additional peaks due to hexagonal TPP. All ^{13}C resonances of included molecular rotors are upfield shifted with respect to $CDCl_3$ solutions. Saturated samples contain an additional set of peaks due to guest molecules located outside TPP channels, with chemical shifts comparable to those of neat guests.

In all cases, both ^{31}P CP MAS and ^{31}P SPE NMR spectra contain a single signal with a chemical shift ~32 ppm, characteristic of hexagonal TPP.

*Rotor **1***. The ^{13}C NMR spectrum of **1** in $CDCl_3$ solution (Figure 3A) consists of seven well resolved peaks (Table S3 in Supporting Information and Chart 1). Two are due to the *tert.*-Bu group (29.9 ppm for CH_3 and 37.2 ppm for C), one at 88.8 ppm (C≡C), and four at 122.5, 130.0, 144.9, and 169.2 ppm (pyridazine). Almost all of these peaks are slightly shifted downfield in the ^{13}C CP MAS NMR spectrum of neat solid **1** (Figure 3B).

The ^{13}C CP MAS NMR spectrum of the unsaturated inclusion 30%**1**@TPP-d_{12} (Figure 3C) resembles some of the features of the spectrum of neat **1**, but also contains three additional peaks marked as TPP, which are due to the three crystallographically unequivalent aromatic carbon atoms present in hexagonal TPP-d_{12}. The triple bond carbon atom at 88.8 ppm in solution is not visible in the inclusion because of inefficient cross-polarization dynamics caused by its longer distance from protons. All remaining carbon resonances of the guest molecule are shifted upfield by 0.5 to 3.2 ppm relative to the isotropic spectrum in $CDCl_3$ solution.

A slight excess of **1** in the saturated inclusion 40%**1**@TPP-d_{12} (Figure 3D) gives rise to three additional peaks in the ^{13}C CP MAS NMR spectrum, which represent all three structural motifs in compound **1**: the pyridazine core (C at 169.2 ppm), the triple bond (C at 89.6 ppm), and the *tert.*-Bu group (C at 37.5 ppm). All these peaks have identical or slightly upfield shifted chemical shifts relative to **1** in solution. The remaining four resonances of unincluded guest molecules are overlapped either with TPP signals or with peaks of included **1**. The peaks marked with an asterisk in Figure 3 (panels B, E, F, G, and H) are spinning side bands.

The ^{31}P CP MAS NMR spectra of both 30%**1**@TPP-d_{12} and 40%**1**@TPP-d_{12} (Figure 3E and G) contain one singlet at ~32 ppm, which is visible because of polarization transfer from included hydrogen atom carrying guest molecules. The corresponding ^{31}P SPE NMR spectrum (Figure 3F and H) also consists of one peak at ~32 ppm, which originates from three crystallographically equivalent phosphorus nuclei present in hexagonal TPP-d_{12}.

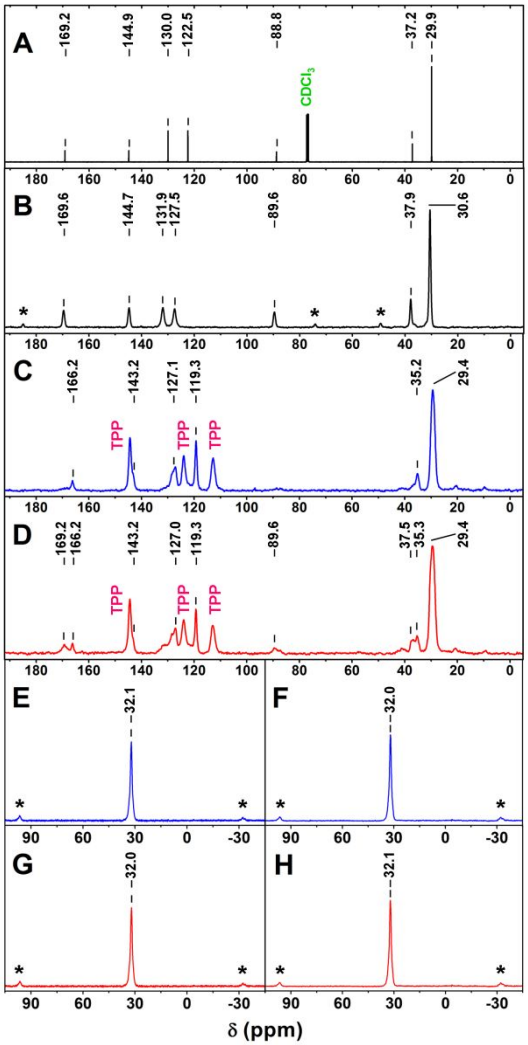

Figure 3. ^{13}C NMR spectrum of **1** in solution (A), ^{13}C CP MAS NMR of neat **1** (B), 30%**1**@TPP-d_{12} (C), and 40%**1**@TPP-d_{12} (D). ^{31}P SPE NMR: 30%**1**@TPP-d_{12} (E), 40%**1**@TPP-d_{12} (G), and ^{31}P CP MAS NMR: 30%**1**@TPP-d_{12} (F), 40%**1**@TPP-d_{12} (I). Asterisks label spinning side bands.

Rotor 2. Compound **2** consists of four characteristic units (*tert.*-Bu groups, pyridazine cores, triple bonds, and BCP cage), all easily identifiable in the ^{13}C NMR spectrum in $CDCl_3$ solution (Figure 4A and Table S3 in Supporting Information).

In the ^{13}C CP MAS NMR spectrum of neat **2**, all carbon atom resonances are doubled, except for signals of the BCP cage and the *tert.*-Bu group (Figure 4B), indicating that two crystallographically different environments are present in the unit cell. The signal of the BCP quaternary bridgehead carbon atoms is overlapped with three equivalent methyls of the *tert.*-Bu group.

The ^{13}C CP MAS NMR spectrum of the unsaturated inclusion 15%**2**@TPP-d_{12} contains three additional peaks due to TPP (Figure 4C). All four pyridazine carbon resonances are shifted upfield (165.6, 143.2, 127.0, and 119.0 ppm) relative to the solution NMR spectrum (168.4, 145.4, 129.4, and 122.2 ppm). Both C≡C signals are present in the

solution spectrum at 77.3 and 91.6 ppm, but are absent in the spectrum of 30%**2**@TPP-d_{12}. Three equivalent CH_2 groups in BCP give one peak at 56.7 ppm, shifted upfield relative to the solution spectrum (58.9 ppm). The same trend is also observed for both resonances of the *tert.*-Bu group (C at 34.2 ppm and CH_3 at 28.5 ppm), which are shielded and thus shifted upfield relative to ^{13}C NMR of **2** in $CDCl_3$ solution (37.0 and 29.9 ppm).

The ^{13}C CP MAS NMR spectrum of the saturated inclusion 30%**2**@TPP-d_{12} is more complex than that of the unsaturated sample 15%**2**@TPP-d_{12} (Figure 4D), because it contains additional four signals (one pyridazine C at 168.9 ppm, a weak C≡C signal at 77.3 ppm, three equivalent CH_2 groups of the BCP cage at 59.0 ppm, and C of the *tert.*-Bu group at 36.9 ppm). They arise from an excess of **2**, located outside the TPP channels. The signals of the remaining carbon atoms of unincluded **2** are overlapped with either TPP resonances or those of included **2**.

The ^{31}P SPE and ^{31}P CP MAS NMR of both 15%**2**@TPP-d_{12} and 30%**2**@TPP-d_{12} (Figures 4E - H) again contain only one singlet at ~32 ppm. This shows that both inclusion compounds contain only the hexagonal form of TPP and that hydrogen atom carrying guest molecules are located in the close proximity to the phosphorus nuclei.

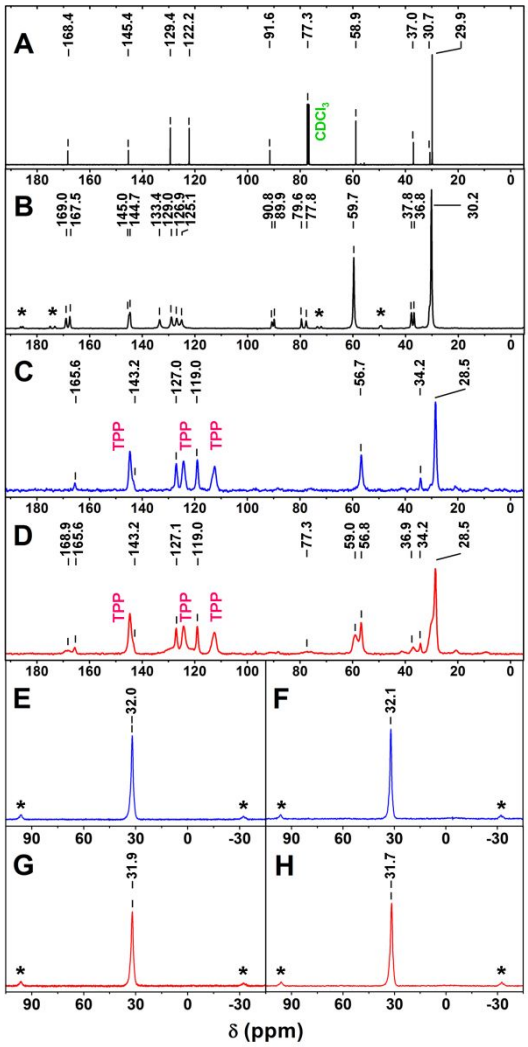

Figure 4. ^{13}C NMR spectrum of **2** in solution (A), ^{13}C CP MAS NMR of neat **2** (B), 15%**2**@TPP-d_{12} (C), and 30%**2**@TPP-

d_{12} (D). ^{31}P SPE NMR: 15%**2**@TPP-d_{12} (E), 30%**2**@TPP-d_{12} (G), and ^{31}P CP MAS NMR: 15%**2**@TPP-d_{12} (F), 30%**2**@TPP-d_{12} (H). Asterisks label spinning side bands.

Compounds **3**, **4**, and **5** differ from **2** only in the numbers and/or positions of triple bonds. Their ^{13}C and ^{31}P NMR spectra and spectra of their inclusion compounds were interpreted in an analogous manner and do not require additional comments. The spectra and ^{13}C chemical shifts are listed in Table S3 and Figures S3, S4, and S5 (Supporting Information).

(ii) Cross-polarization (CP) Dynamics. The CP dynamics was studied for **2** and its inclusion complex 15%**2**@TPP-d_{12}. The dependence of the individual signal intensities on the length of CP contact time was measured in the range of 0.5 - 9 ms.

The signals of protonated carbon atoms *a*, *f* and *g* in the spectra of neat **2** have more than 50% of their maximum intensity already after a contact time of 0.5 ms (Chart 1 and Figure 5A). This behavior is expected because the molecules of **2** do not exhibit any sign of dynamics in their NMR spectra and the carbon nuclei are therefore strongly coupled to the directly attached hydrogen atoms. The signals of carbon atoms *e*, *h* and *i*, which are two bonds away from a hydrogen atom, have low intensity after a 0.5 ms contact time, but this intensity grows rapidly as the contact time increases. This observation fits slower CP dynamics associated with the longer distance to the nearest hydrogen atom (~2.2 Å). The signals of triple bond carbon atoms *c* and *d*, which are separated by three bonds from the nearest hydrogen atoms, grow even more slowly with increasing contact time (Chart 1 and Figure 5A). This is the result of inefficient CP given by even longer C-H distances. The *c* and *d* carbon atoms are separated by 2.7 and 3.1 Å, respectively, from the nearest hydrogen atom in the same molecule of **2**; this distance is comparable with the closest intermolecular contacts with hydrogen atoms (e.g. 2.9 Å between *c* and hydrogen atoms attached to carbon atom *a* from a neighboring molecule) and in this case both intra- and inter-molecular CP probably contribute to the signal. The slowest growth with increasing contact time is observed for the signal of the *tert*-butyl carbon atoms *j*. It is known that rapid rotation of *tert*-butyl groups attenuates the CP process.[39]

In the ^{13}C CP MAS spectra of 15%**2**@TPP-d_{12}, new signals corresponding to the carbon atoms of TPP are present (Figure 4). Similarly as in neat **2**, signals of the protonated carbons *a*, *f* and *g* have high intensity already at short contact times (Chart 1 and Figure 5B). Carbon atoms *h* and *i* separated by two bonds from the nearest hydrogen atom exhibit a weak signal at short contact times, but this signal grows rapidly at longer contact times (the signal of *e*, also separated by two bonds from a hydrogen atom, is hidden under one of the signals of TPP). The signal of *tert*-butyl carbon atoms *j* also exhibits a slow increase of intensity due to insufficient CP. The most remarkable difference in the variable contact time experiments on neat **2** and 15%**2**@TPP-d_{12} is observed for the signals of the triple bonds *c* and *d*, whose intensity increases very slowly with increasing contact time. This observation may be attributed to insufficient intramolecular CP from the closest hydrogen nuclei, further attenuated by fast rotation of the pyridazine rings that leads to smaller C-H coupling and, furthermore, by the absence of intermolecular interactions with hydrogen atoms. The attenuated signals of the triple bonds may thus serve as additional evidence for the formation of an inclusion complex. The signals of TPP also grow at a similar slow rate and this indicates that the shortest distance between TPP carbon atoms and the hydrogen atoms of **2** is similar to that between the triple bond carbon atoms and the closest hydrogen atoms (ca

3.0 Å). Note also that the changes in signal intensities upon the formation of the inclusion compound are not caused by different relaxation behavior of the signals. All the variable contact time experiments were performed with the repetition time of 4 s, but a control experiment with a repetition time of 30 s provided similar signal intensities as that with the 4 s repetition time for both **2** and 15%**2**@TPP-d_{12}.

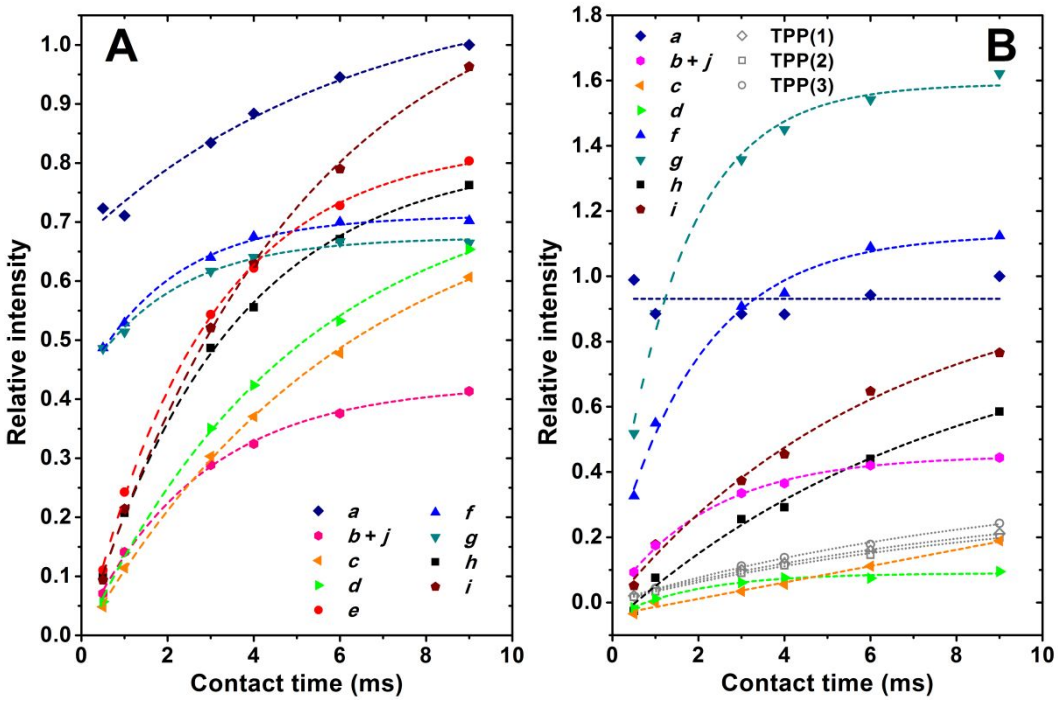

Figure 5. The dependence of relative ^{13}C CP MAS signal intensity (normalized to the maximum intensity of *a*) on the contact time for crystalline **2** (A) and 15%**2**@TPP-d_{12} (B).

The triple-bond carbon signals can be observed in ^{13}C NMR spectra of the inclusion compounds acquired with direct carbon excitation without CP. This is documented in Figure 6 for compound **5** and its inclusion complex 15%**5**@TPP-d_{12}. The triple bond signals are missing in the CP MAS spectrum of 15%**5**@TPP-d_{12} with contact time of 4 ms (Figure 6C), but are clearly present in the spectrum acquired with direct carbon excitation (Figure 6D). Furthermore, the intensity of TPP signals is higher in the direct excitation spectrum because the intensity is not driven by intermolecular C - H interactions any more.

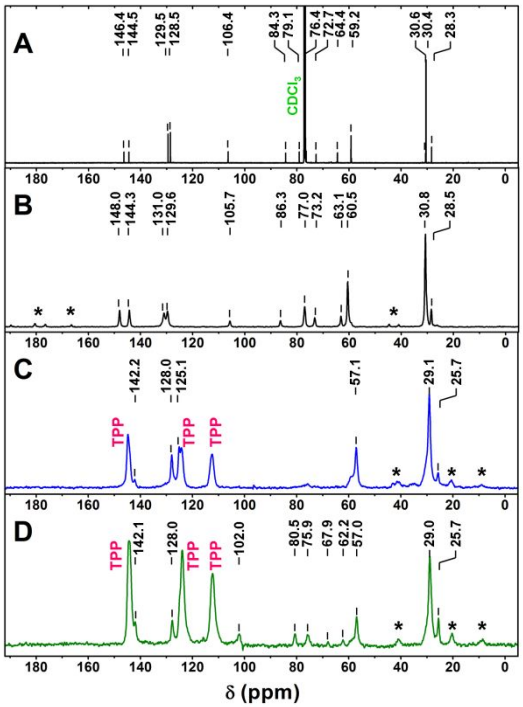

Figure 6. ^{13}C solid-state NMR spectra of **5** in $CDCl_3$ solution (A), neat **5** (B), and 15%**5**@TPP-d_{12} measured with cross-polarization (C) and direct excitation (D) of carbon nuclei.

(iii) Lower Bound for Rotational Frequency. Fast molecular re-orientation in solutions averages anisotropic chemical shielding to a single isotropic value. In solids molecular reorientation is suppressed and NMR spectra of static powder samples consist of broad lines that correspond to sums of signals from nuclei with all possible orientations relative to the magnetic field direction. Rotation of the sample at the magic angle (54.7°) with respect to this direction partially averages the molecular orientations and the broad solid-state NMR signals break up into a set of lines separated by the spinning frequency. Magic angle spinning (MAS) at high frequencies leaves only the isotropic line in the spectrum accompanied by a few low-intensity spinning side-bands (SSBs). Molecular mobility in the solid material leads to a suppression of the chemical shift anisotropy[40] and therefore, the number and intensity of SSBs may be used to diagnose internal motion.

In the room-temperature ^{13}C NMR spectra of neat rotors acquired at 13 kHz MAS, the dominant lines are those corresponding to isotropic chemical shifts and the few observed SSBs belong mostly to the signals of triple bonds carbons, which have a very large chemical shift anisotropy. However, when the spectra are acquired at 4.3 kHz MAS, SSBs associated with all carbon signals appear. In many cases, the SSBs have even higher intensity than the signals at isotropic chemical shifts, as illustrated for **5** in Figure 7. The lowest intensity SSBs are those associated with the CH_2 carbon atoms of the BCP cage and CH_3 carbon atoms of the *tert*-butyl groups, due to rotational mobility of these groups in the crystalline state of neat **5**. On the other hand, many SSBs are present in the signals of the pyridazine carbon atoms, which indicates that these aromatic rings do not undergo π jumps or any kind of rotation.

In the spectrum of the inclusion complex 15%**5**@TPP-d_{12} acquired at 13 kHz MAS, only very few SSBs are present and they belong to the signals of TPP (black asterisks in

Figure 7C). In the spectrum acquired at 4.3 kHz, many more SSBs appear and are mostly due to TPP (Figure 7D). The SSBs associated with **5** have very low intensity or are missing altogether. This observation confirms the formation of an inclusion complex; the TPP host is rigid and provides signals with many SSBs in slow MAS spectra, but the guest molecule is relatively mobile and rapidly reorients all of its parts, thus suppressing the effect of chemical shift anisotropy and reducing the number of SSBs. This suppression shows that the speed of the molecular reorientation is at least comparable to chemical shift anisotropy expressed in Hz or faster, thus setting the lower limit of the rotational rate at ~10 kHz at 300 K.[40,41] It is likely that the other rotors behave similarly since (i) the interior of the TPP channel is the same in all cases, (ii) almost all rotors (except **1**) shares the same building blocks (*tert.*-Bu, BCP, pyridazine rings, triple bonds) and differ only in length and (iii) experimentally obtained rotational barriers are distributed in quite narrow region.

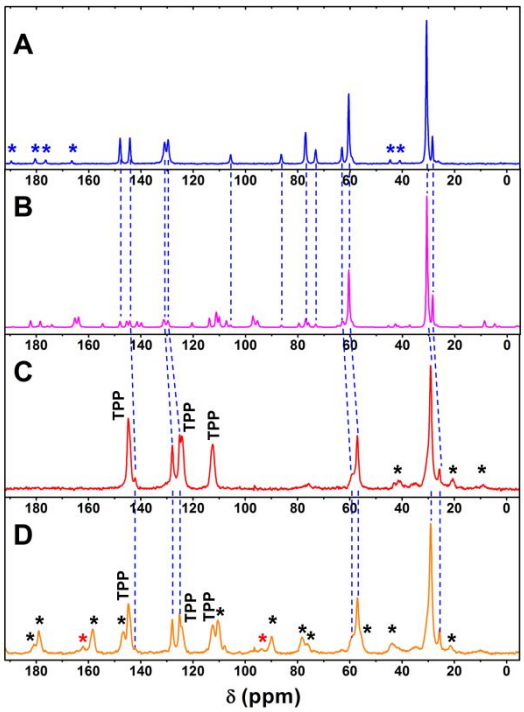

Figure 7. ^{13}C CP-MAS spectra of **5** and 15%**5**@TPP-d_{12} measured with 13 kHz (A and C) and 4.3 kHz MAS (B and D). The blue dashed lines connect the isotropic lines in the spectra of **5** and the asterisks indicate the SSBs (black for TPP signals and red for 15%**5**@TPP-d_{12} signals).

Differential Scanning Calorimetry (DSC). The samples were analyzed in a cyclic mode starting by heating from room temperature to 310 °C, followed by cooling to 40 °C, and heating to 310 °C again. Since all samples decomposed before reaching 310 °C the subsequent cooling and heating cycles resulted in featureless traces. Therefore, only the first heating curves are shown in Figure S1 (Supporting Information).

The trace of neat hexagonal TPP-d_{12} agrees with previously published data.[42] The inconspicuous broad exotherm with a maximum at ~130 °C is due to a first-order transition of hexagonal TPP-d_{12} into its more stable monoclinic form. The endotherm at 220 °C is

associated with a transition of monoclinic TPP-d_{12} into its hexagonal form and the intense endotherm at 247 °C is due to melting.

In general, DSC traces of the neat guests **1** - **5** (blue lines B, D, F, H, and J in Figure S1) revealed that only the shortest rotor **1** melts. The BCP containing compounds **2** - **5** decomposed without melting as demonstrated by strong exotherms in their DSC traces. Not surprisingly, extension of the guest length by addition of triple bonds decreases the stability of the compounds: the shortest BCP based rotor **2** decomposes at ~290 °C and the longest rotor **5** with four more triple bonds already at ~240 °C. Compounds **4** and **5** detonate during DSC analysis.

The DSC traces of inclusion compounds usually consist of an endotherm attributed to melting at ~245 °C, which is overlapped with a broad exotherm peak at 240-290 °C corresponding to decomposition of the guest molecules. See Supporting Information for detailed description of individual DSC traces.

Powder X-Ray Diffraction. X-ray powder patterns were acquired for all ten inclusion compounds (Table 2). All the samples showed patterns consistent with a hexagonal bulk inclusion compound with the lattice parameters and uncertainties listed in the Table 3. The hexagonal structure is characterized by two equal "in-plane" lattice parameters *a* (Å), and a distance between planes *c* (Å). No unassigned peaks appear in any of the patterns with the exception of 25%**5**@TPP-d_{12}, which has a single broad peak of unknown origin located at q = ~1.5 Å^{-1}, consistent with a lattice spacing of roughly 4.2 Å (Figure S6 in Supporting Information).

Table 3. Hexagonal lattice parameters for inclusion compounds.[a]

Cmpd.	Inclusion	a (Å)	c (Å)
1	30%**1**@TPP-d_{12}	11.770 ± 0.001	9.948 ± 0.002
	40%**1**@TPP-d_{12}	11.838 ± 0.001	10.021 ± 0.002
2	15%**2**@TPP-d_{12}	11.811 ± 0.001	9.908 ± 0.001
	30%**2**@TPP-d_{12}	11.853 ± 0.001	9.930 ± 0.001
3	20%**3**@TPP-d_{12}	11.693 ± 0.001	9.980 ± 0.002
	25%**3**@TPP-d_{12}	11.715 ± 0.001	10.026 ± 0.002
4	15%**4**@TPP-d_{12}	11.736 ± 0.001	9.960 ± 0.001
	30%**4**@TPP-d_{12}	11.757 ± 0.001	9.994 ± 0.002
5	15%**5**@TPP-d_{12}	11.673 ± 0.001	9.926 ± 0.001
	25%**5**@TPP-d_{12}	11.717 ± 0.001	9.968 ± 0.002

[a] Lattice parameters for guest free hexagonal TPP: a = 11.454(5) Å, and c = 10.160(5) Å.[43]

Figure 8 represents a characteristic diffractogram of bulk inclusion in hexagonal TPP (15%**2**@TPP-d_{12}). All remaining diffractograms are shown in the Supporting Information (page S10, Figure S6).

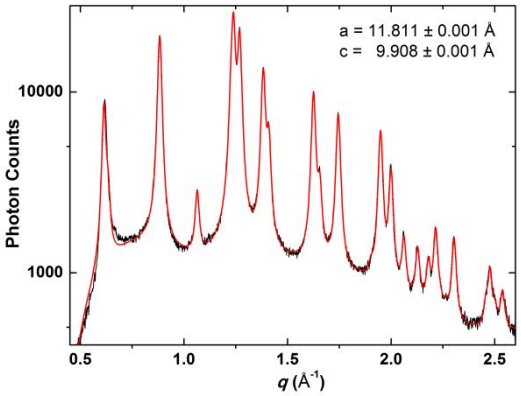

Figure 8. PXRD of 15%**2**@TPP-d_{12}.

Dielectric Spectroscopy. We measure the motion of the dipole rotators in the inclusion compounds directly by loading powdered inclusion material onto the surface of a thin-film interdigital capacitor (see Supporting Information) and then measuring the frequency- and temperature-dependent electric susceptibility as the difference between the inclusion-loaded and the original empty capacitor. The "in-phase" or real part of the capacitance measures the ability of the material to produce a dipole moment per unit volume while the "out-of-phase" or imaginary part of the capacitance measures dielectric energy loss processes.

All ten inclusion compounds (Table 2) show characteristic dielectric loss peaks and changes in the capacitive response. Figure 9 shows the real part and imaginary part of the capacitance for 30%**1**@TPP-d_{12}. We found a single loss peak, an associated drop in the real part, consistent with freezing out of the dipole reorientation, and frequency-dependent differences in the response that are qualitatively consistent with Arrhenius thermal activation over barriers. Simultaneous fitting of the data sets to the Debye model of independent dipoles for populations of 9-state rotors (described in detail in the Discussion section) allows us to extract a distribution of activation energy barriers to dipole rotation around two central values of 2.4 ± 0.1 kcal/mol and 2.0 ± 0.1 kcal/mol, and a central attempt time of 0.5×10^{-13} s. The two populations both favor the anti-ferroelectric alignments of local dipoles. The two populations differ in that one shows an asymmetry of roughly 106 K (listed as A in Table 4 to indicate an anti-ferro aligned 9-state), while the other is indistinguishable from non-interacting dipoles. Two populations of dipoles are found for all ten inclusion compounds. Their barrier heights, attempt times, and asymmetries are listed in Table 4.

Table 4. Dipole rotation parameters - logarithm of the attempt times (log τ_0), energy barriers (E_B), and barrier asymmetries (S). Letter "A" and "F" represents systems allowing antiferro- and ferro-alignement.

Cmpd.	Inclusion	log τ_0[a]	E_{B1} (kcal/mol)[b]	S_1 (K)[c]	E_{B2} (kcal/mol)[b]	S_2 (K)[c]
1	30%**1**@TPP-d_{12}	-13.7	2.4	105 (A)	2.0	0 (A/F)
	40%**1**@TPP-d_{12}	-13.5	2.5	118 (A)	2.1	0 (A/F)
2	15%**2**@TPP-d_{12}	-12.2	2.7	147 (A)	2.1	32 ± 6 (F)
	30%**2**@TPP-d_{12}	-13.7	3	167 (A)	2.4	42 ± 20 (F)

3	20%**3**@TPP-d_{12}	-13.0	3.2	118 (A)	2.4	40 ± 40 (F)
	25%**3**@TPP-d_{12}	-13.2	3.3	120 (A)	2.6	0 (F)
4	15%**4**@TPP-d_{12}	-13.0	2.1	184 (A)	2.3	57 (A)
	30%**4**@TPP-d_{12}	-12.2	1.9	209 (A)	2.1	72 (A)
5	15%**5**@TPP-d_{12}	-12.6	3.5	176 (A)	2.9	38 (A)
	25%**5**@TPP-d_{12}	-12.8	3.2	229 (A)	2.9	74 (A)

Standard error is: [a] ± 0.2, [b] ± 0.1 kcal/mol, [c] ±5 K.

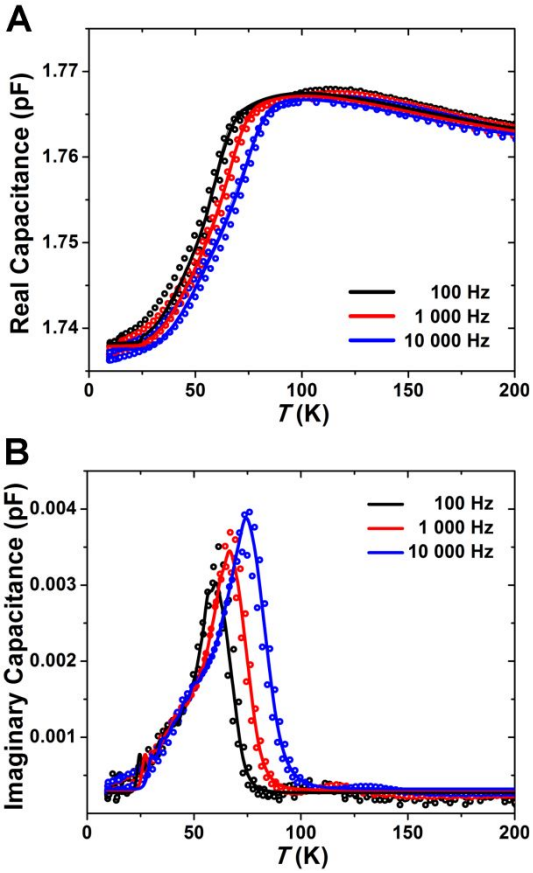

Figure 9. Dielectric loss of 30%**1**@TPP-d_{12} between 10 and 250 K. Black, 100 Hz; red, 1 000 Hz; blue, 10 000 Hz. Real (A) and imaginary (B) capacitance.

Relative dielectric susceptibility for the five saturated inclusions as a function of temperature is displayed in Figure 10. For comparison with the TPP background, we also show the dielectric susceptibility temperature dependence for an inclusion of benzene, a nonpolar aromatic hydrocarbon (benzene@TPP-d_{12}). All data sets are at 10 kHz.

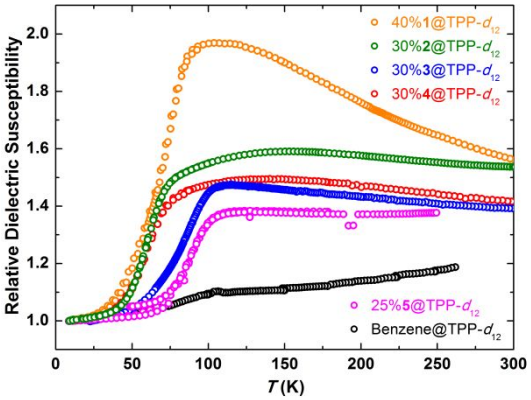

Figure 10. Relative dielectric susceptibility for five polar saturated inclusion compounds (40%**1**@TPP-d_{12}, 30%**2**@TPP-d_{12}, 30%**3**@TPP-d_{12}, 30%**4**@TPP-d_{12}, and 25%**5**@TPP-d_{12}), and nonpolar inclusion compound of benzene@TPP-d_{12}.

Calculations. To obtain a rough representation of the time-averaged rotational potential in which the two pyridazine rings of a rotor molecule move and to minimize the effects of TPP lattice truncation, a model was used in which a central TPP channel containing the rotor under study (shown in orange in Figure S8 in Supporting Information) was surrounded by six other channels and all seven channels are filled with molecules of **1**. Completely relaxed geometry optimization was performed for a slab consisting of four layers of TPP by the MP6-D3H4[34] method, which includes van der Waals interactions. The instantaneous geometry obtained in this manner does not have three-fold symmetry, whereas the time-averaged system does. To obtain an approximation to the symmetric time-averaged potential, the sixteen models shown in Figure S9 were averaged (in these models, the central pyridazine is replaced with 1,2,4,5-tetrazine, similar in shape to pyridazine, but without a dipole moment and structural distortion). The geometries of the six outer channels and their guests (shown in blue) that were obtained in this fashion were then fixed at the averaged values. The dihedral angles φ_1 and φ_2 of the two pyridazine rings of **1** were fixed in steps of 15° and the remainder of the central TPP channel was fully relaxed to locate the optimal conformation of **1**. The rotational potential was calculated as a function of φ_1 and φ_2. The simulations were performed with the program MOPAC2016.[44] The computational procedure is crude compared with a possible more demanding molecular dynamics treatment but is expected to provide an idea of the potential energy surface for pyridazine rotation.

Figure 11A shows the approximate contour lines of a such a surface calculated by the B97-D3/SVP method[35] for the two-dimensional subspace of geometries defined by the rotational dihedral angles φ_1 and φ_2 (measured clockwise) that the two pyridazine rings of **1** inserted into the central channel form with respect to a line that bisects two opposite edges of the hexagon formed by the channel walls when viewed along the channel axis (at $\varphi_1 = \varphi_2$, the planes of the pyridazine rings are parallel and their dipoles point in the same direction). All other geometrical degrees of freedom in the central channel are optimized.

The nine minima in the potential energy surface are surrounded by dark blue contour lines and are located close to φ_1 values of 90, 210, and 330, and φ_2 values of 30, 150, and 270. The maxima are surrounded by dark red lines. The shape of the surface exhibits three-fold symmetry with respect to both φ_1 and φ_2. The expected (see Supporting Information) nine low-energy conformations differing by ~60° between the two pyridazine rings located in

adjacent layers of TPP are clearly present. To facilitate visualization, Figure 11 also shows views along the channel direction of the dipoles associated with the two pyridazine rings (a green and an orange arrow) at selected values of φ_1 and φ_2 (minima in black and saddle points in green hexagons).

In measurements of dielectric losses, Debye peaks are expected for those jumps between conformations that change the projection of the molecular dipole moment of **1** into the direction of the electric field. The field direction was chosen to be perpendicular to the channel axes and parallel to the reference direction from which φ_1 and φ_2 are measured. In Figure 11B, we provide a map of the magnitude of this projection (in Debye) as a function of φ_1 and φ_2. Those jumps that connect φ_1 and φ_2 values that differ in color should produce signals. Examples are jumps from (330,30) to (330,150) and to (210,30).

Jumps connecting values of the same color should be silent in dielectric spectra. An example is a jump from (210,150) to (210,270). Jumps from one minimum to another are easiest along lines passing through saddle points. These lines are oriented roughly vertical or horizontal, implying that only one of the pyridazines prefers to rotate at a time. The transition states separating two energy minima are located in regions defined by light blue and cyan contour lines and lie 4 - 5 kcal/mol above the minima; activation energies are expected to be somewhat lower. For example, the saddle point at (140,150) interconnects minima at (90,150) and (210,150).

A B97-D3/SVP calculation in a six-layer TPP model for the energy profile for sliding a molecule of **1** from one position to the next within the TPP channel, with pyridazine rings relaxed to their best orientations at each point along the channel axis, showed a relatively high barrier of ~10 kcal/mol. It thus appears that the motion of **1** along the axis is much slower than rotation of its rings, which only has a barrier of about 4 - 5 kcal/mol. As a result of an unsymmetrical optimal location of **1** with respect to the center of the TPP layer, the two pyridazine rings have different environments and the rotation angles φ_1 and φ_2 remain inequivalent.

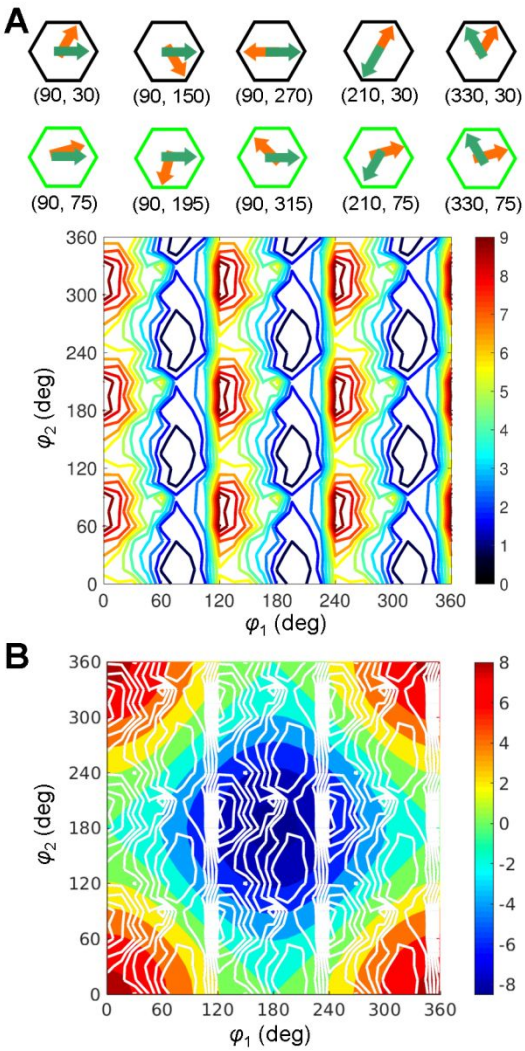

Figure 11. A: B97-D3/SVP calculated potential energy surface (in kcal/mol) for rotation of **1** inserted in the central channel of a four-layer TPP slab surrounded by six other channels filled with **1**. The two-dimensional subspace of geometries shown is defined by the rotational angles φ_1 and φ_2 (see text). Above, examples of dipole orientations at various rotational angles φ_1 and φ_2, viewed along the channel axis. B: Projection of the molecular dipole moment of **1** in Debye into the direction $\varphi_1 = \varphi_2 = 0$.

DISCUSSION

Synthesis. Preparation of rotor molecules **2** - **5** is an extension of the already well developed chemistry of 1,3-diethynylbicyclo[1.1.1]pentane (**17**)[18,37,38,45,46,47,48,49] and thus does not require much comment. Two issues will be mentioned briefly.

(i) The nonvolatile and bench-stable silyl derivative **16** was identified as a very useful source of the volatile diyne **17**, which is explosive in crystalline state. Compound **17** can be liberated from **16** *in-situ* using TBAF in THF. This completely avoids manipulation of the

volatile and potentially dangerous diyne **17** and significantly simplifies further synthetic operations.

(ii) The tetrayne **18**, readily available from the diyne **16** in four synthetic steps using Corey-Fuchs synthesis, was purified by chromatography on silica gel with pentane. This purification significantly improved the yields of subsequent synthetic steps. It is advisable to store the strained tetrayne **18** with a small amount of solvent, since it undoubtedly is a highly energetic compound, and it is strongly recommended to perform all manipulations with it only in solution. Solid microcrystalline **18** spontaneously detonates at temperatures above ca 85 °C (attempted determination of melting point of three tiny crystals with total weight <1 mg caused a detonation comparable with that of ca 30 mg of NI_3). It is expected that mechanical stress including crushing of larger crystals can initiate explosion even at much lower temperatures.

Inclusion Compounds. TPP is known to be available in two crystal structures.[50] A monoclinic form is the stable phase for pure TPP at ambient conditions up to ~150 °C and has no free space for guest inclusion. A hexagonal form is the stable phase above ~150 °C for pure TPP and is the structure adopted upon inclusion of guests at any temperature. The included guest molecules stabilize it against collapse to the monoclinic form.[51,52] The observed powder X-ray patterns of the inclusion compounds show only the hexagonal structure and no evidence for the presence of any monoclinic TPP. All samples show a 2 - 3% expansion of the in-plane lattice parameter *a* and a small contraction (1 - 2%) of parameter *c*, the distance between layers. This agrees with the expected structures of bulk inclusions, because guest molecules in general cause a small in-plane expansion of the TPP host matrix.[18,19,27,28] In cases where the guest mole fraction is higher than expected for complete inclusion, peaks associated with crystals of the neat rotor molecules were not detected. Perhaps the excess guest molecules remain amorphous.

The inclusions of compound **2** produce the largest in-plane lattice parameters (Table 3), which indicates more available space in the TPP channels. This may be an important contribution to the lower rotational barriers also found for this case.

The TEM analysis revealed that the morphology of 30%**1**@TPP-d_{12}, which was chosen as representative example, is comparable with previously prepared bulk inclusions.[28] The sample consists of disc-shaped particles with ~50 nm diameter and ~25 nm thickness. One ideal and defect-free discoidal TPP particle with such size can accommodate ~24 000 molecules of rotor **1** or ~14 000 molecules of **5** (see Supporting Information for additional detail).

Solid-State NMR. The methods discussed so far provided information regarding basic properties of the inclusion compounds and yielded some hints about the surface vs. bulk type of inclusion, but were not able to distinguish between unsaturated and saturated samples, nor did they provide information about positions of the guest molecules inside TPP channels. Solid-state ^{31}P and ^{13}C analysis of all samples answers these questions.

All solid-state ^{31}P SPE NMR spectra contain only one singlet at ~32 ppm, corresponding to three crystallographically equivalent phosphorus nuclei present in hexagonal TPP, and thus reveal exclusively the hexagonal form of TPP. No traces of the monoclinic polymorph of TPP were detected, in agreement with PXRD.

The ^{31}P CP MAS NMR spectra of all samples again consist of a single peak at ~32 ppm, due to transfer of polarization from hydrogen atoms attached to guest molecules located in close proximity to the phosphorus nuclei. ^{13}C CP MAS spectra provide additional strong evidence confirming our identification of the materials as bulk inclusions. In unsaturated samples, the chemical shifts of all carbon atoms of the guest molecules were upfield shifted

relative to samples in $CDCl_3$ solutions (Table S3 in Supporting Information), and this is attributable to shielding by neighboring phenyl rings of TPP molecules. On the other hand, saturated samples provided two sets of peaks: one upfield shifted and assigned to included guest molecules, and the other with almost unshifted resonances with respect to $CDCl_3$ solutions and assigned to rotor molecules located outside the TPP crystallites. All solid-state ^{13}C CP MAS NMR spectra of inclusion compounds also contain three additional peaks due to the TPP matrix, and this is an additional proof that hydrogen atom carrying rotor molecules are inserted inside TPP channels, because during cross-polarization (CP) experiments polarization is transferred not only to carbon atoms of guests, but also to carbon atoms of neighboring perdeuteriated TPP molecules.

The ^{13}C CP MAS NMR spectra of all BCP carrying unsaturated inclusions are characterized by attenuation or complete absence of triple bond carbon signals located next to the BCP cage. This phenomenon, which was already observed several times in the past,[18,19,27] but was thoroughly studied for the first time now, was attributed to insufficient intramolecular CP from the closest hydrogen nuclei, additionally attenuated by fast rotation of the pyridazine rings that leads to very small C-H coupling inside the TPP channel. The significantly reduced intensity or complete absence of the triple bonds signals may thus serve as additional evidence for the formation of inclusion compounds.

Pyridazine Rotators: Dynamics and Mutual Interactions. The evidence above supports a picture where the double pyridazine molecules are included into the bulk of a hexagonal TPP host. Therefore, the individual pyridazine dipole rotator moieties (i) are constrained to rotate about the axis of the long TPP channels; (ii) are in rotational potential energy environments that are locally three-fold, but where neighboring dipole environments can be either aligned in the three preferred directions or anti-aligned depending on dipole-dipole distance; (iii) have other pyridazine dipole rotators at varying separation along the channels and in neighboring channels; and (iv) are incorporated into the final material with dipole volumetric densities that differ for molecules **1** - **5**. The dielectric behavior that we observe shows the impact of these four points.

We first discuss the scaling of dielectric susceptibility with dipole volumetric density, where models of independent dipoles, most appropriate for describing the high-temperature para-electric phase, predict a direct proportionality between the dipole volume density and the dielectric susceptibility. Fully saturated inclusion compounds of **1** have the most dipoles per unit length and therefore per volume and these dipole density numbers then decrease in sequence from **1** down to **5**. Figure 10 (see discussion in Supporting Information) shows that the relative susceptibility indeed sorts all the inclusion compounds with inclusions of **1** having the largest susceptibility and **5** the smallest. The inclusion compounds of **3** and **4** are interesting cases as they have nearly equal dipole density but different dipole-dipole separations and local structure. Nevertheless, their inclusion compounds have nearly equal susceptibilities at higher temperatures. They also show interesting differences, as do the rest of the inclusion compounds, at lower temperatures, where the local environments and dipole-dipole interactions begin to play an important role.

Important aspects of the lower-temperature dielectric behavior shown by all the inclusion compounds are the dielectric loss peaks in the imaginary component of the dielectric response (Figure 10), the associated Arrhenius transition rates between potential wells with barriers (Table 4), and the associated drop in dielectric susceptibility as the dipoles freeze into local potential wells. Inclusion compounds of **3** and **5** show rotational energy barriers in excess of 3 kcal/mol, whereas inclusions of **1**, **2**, and **4** have barriers below 3 kcal/mol. The higher rotation energy barriers for **3** and **5**, compounds where the pyridazine

moieties are between carbon triple bonds, are consistent with previous observations on rotors of similar structure but carrying a single pyridazine.[28] Rotation about the triple bonds is expected to have very low barriers in the gas phase, but they increase flexibility and accentuate non-linearity that apparently allow the dipolar rotators to interact more strongly with the TPP channel walls. Similarly, the observed barriers near 2 kcal/mol for pyridazine rotators adjoining *tert.*-Bu end groups are consistent with observations on rotors carrying a single pyridazine.[28] Taken together, the observed rotation barrier heights and attempt times all appear to be consistent with the local structure surrounding the pyridazine sections in TPP.

Finally, we turn to a more subtle behavior that appears in the overall temperature dependence of the dielectric susceptibility, and which we suggest arises from the correlated alignment of the local three-fold potentials experienced by different dipolar rotators in TPP. This behavior allows us to measure the impact of dipole-dipole interactions on the dielectric susceptibility. The behavior we observe appears in the real part of the dielectric susceptibility (Figures 9A and 10) and is most obvious in the inclusions of **1**, **2**, and **4**. We observe a systematic tendency of the dielectric susceptibility to slowly arc downwards away from the typical $1/T$ Curie-like behavior predicted for independent dipoles in symmetric well structures. This softening of the initially increasing susceptibility with decreasing temperature takes place over a broad range of temperatures beginning at perhaps 200 K, leads to a maximum in the susceptibility between 100 and 150 K depending upon the particular inclusion, and then decreasing susceptibility at the lower temperatures until dipole rotation is frozen out by the Arrhenius rates. Modeling this type of softening in dipolar susceptibility typically proceeds in terms of potential well structures for the dipolar rotation with one or more lower energy wells for each dipole, wells that eventually capture the dipole population, leading to a decreased equilibrium population of dipoles that can respond to the applied electric field.[53,54,55] The issue in these cases is to understand how particular low energy wells arise naturally in a given system. For the double pyridazine molecules in TPP, the calculations above suggest that the individual dipole rotators move in a locally three-fold set of potential wells. A natural source of local asymmetry in the well depths is provided by the dipole-dipole interactions between either intra- or inter-molecule pairs. In dilute systems, the dominant interaction would be between the two dipoles on one double pyridazine molecule. For denser inclusions, both intra- and inter-molecular interactions and summations of energies over many molecules would be necessary. In all cases, the softening of the dielectric susceptibility in the 100 to 200 K region likely signals that dipole-dipole interactions are leading to asymmetry in the rotational potential wells and thereby suggest that the dipole interaction energies are themselves on the scale of roughly 100 K.

As we discuss further in the Supporting Information, a given dipole rotator and its neighbor, each in its respective three-fold potential, can be modeled as a nine-state system. The TPP environment provides for two distinct types of nine-state situations, involving dipole pairs that are separated along the channel by a distance equal to either an even or an odd multiple of the thickness of a TPP layer. For dipole pairs separated by a distance equal to an even number of TPP layers, the respective three-fold potentials are aligned and allow the dipoles to have aligned orientations for three of the nine states, or to be oriented at 120 degrees to each other in the remaining six states. The three aligned states have high and positive-valued dipole-dipole interaction energy, so are high-energy states overall, with a net dipole moment of twice the single dipole value. The six non-aligned states, each with a net dipole moment equal to the single dipole value, form a polar ground-state manifold. At low temperatures, these six polar states allow for a dipole contribution to the dielectric susceptibility. By comparison, for dipole pairs separated by a distance equal to an odd

number of TPP layers, the respective three-fold potentials for the dipole pair are rotated 60° relative to each other. That orientation allows for three of the nine states to have anti-aligned dipoles, no net dipole moment, and a negative dipole-dipole interaction energy so that these three states form a non-polar ground state manifold. The six non-anti-aligned states have equal energy that is higher due to the dipole-dipole interactions, have a net dipole moment of $\sqrt{3}$ of the single dipole moments, and can contribute to the dielectric susceptibility at higher temperatures. The full inclusion system will, of course, be composed of large numbers of dipole pairs of various separations. However, the main message is that for dipole pairs along the channels with neighbors an odd number of TPP layers apart (e.g., the intra-molecular separation for inclusions of **1**), dipoles can fall into a low-energy non-polar anti-aligned configurations that will reduce the dielectric susceptibility. Even pairs with even layer separation (e.g. neighboring dipoles in saturated inclusions of **2**) will show a decreased number of available polar states at low temperatures.

We have developed two simple statistical mechanics models for these two different nine-state local models to demonstrate the behavior described above under the assumption that only the dipole-dipole interactions contribute to the energy asymmetries of the various configurations. Assuming that the asymmetry is due to dipolar interactions between dipoles some distance a apart the models yield predicted dipolar contributions to the dielectric susceptibility for odd number of layers separation, χ_{odd}, and even number of layers separation, χ_{even}, according to Equations 1.

$$\chi_{odd} \approx (N/V)(p^2/3k_BT)\{3(e^{-S/2k_BT})/[2(e^{-S/2k_BT}) + e(+S/k_BT)]\} \quad (1)$$

$$\chi_{even} \approx (N/V)(p^2/3k_BT)\{[(e^{+S/2k_BT}) + 2(e^{-S/2k_BT})]/[2(e^{+S/2k_BT}) + e(^{-S/k_BT})]\}$$

$$S \approx 3p^2/8\pi\varepsilon\varepsilon_0 a^3$$

Each shows the expected proportionality to dipole density, the typical Curie-like $1/T$ increase with decreasing temperature, and a quotient that describes the equilibrium populations of the nine states. The odd-layer quotient approaches zero at low temperatures as dipoles populate the three-state non-polar ground state manifold. The even-layer quotient approaches a finite value of one-half, as dipoles populate the six-state partly polar ground state manifold. These susceptibilities obtain until low enough temperatures where the kinetics of barrier crossing freeze out dipole motion entirely. The susceptibility functions are identical for zero asymmetry, where they agree with the classical results of Debye[56] and Fröhlich.[57] Finite asymmetry leads to a suppression of susceptibility for the odd layer case, while the even case retains the Curie-like behavior.

Table 5 lists the expected intra- and inter-molecular dipole-dipole separations for **1** □ **5** for saturated inclusions. None of the intramolecular separations are perfect integer multiples of the TPP layer spacing. Still, our calculations for the energy surface of **1** (Figures 11) show that the picture of three-fold wells separated by 120° is accurate. Under the assumption that fractional deviations from perfect integer layer separation are similarly accommodated for the longer double pyridazine molecules, Table 5 lists the type of local dipole-dipole ground state configuration we would expect for both the intra- and inter-molecular dipole pairs. The result clearly shows that we expect a softening of the dielectric susceptibility below the Curie-like $1/T$ very much as we observe. We fitted the real and imaginary parts of the capacitance data to a model that is a superposition of the two susceptibility functions above. This model takes into account the possibility of both local

non-polar configurations and residual partially polar configurations. We find a satisfactory description of the overall temperature-dependent shape of both the real and the imaginary parts as shown e.g., in the fitting of Figure 9. The fitting results listed in Table 4 are in very good qualitative agreement with dipole-dipole interaction energies for the nearest neighbor dipoles in the 100 to 200 K range (S_1 in Table 4). These systems settle into the anti-aligned configurations with decreasing temperature and lead to the drop in dielectric susceptibility. The fitting results suggest that they then leave behind a population of more widely separated dipoles (lower observed anisotropy energy S_2 in Table 4) that then contribute to dielectric susceptibility until the residual rotation barriers prevent dipole motion at the lowest temperatures.

Table 5. Estimated intra-molecular (within one double pyridazine molecule) dipole-dipole spacing and inter-molecular dipole-dipole spacing (between nearest neighbor double pyridazine molecules at saturation of the inclusion) in units of the single TPP layer spacing of 5 Å. Included is an estimate listed as either (Aligned) or (Anti-aligned) about whether the local intra-molecule and neighboring inter-molecule dipoles are in three-fold potential wells that allow for dipole alignment (an even number of TPP layers) or allow for dipoles to be anti-aligned (an odd number of TPP layers).

Cmpd.	Intra (layers)	Inter (layers)
1	1.3 (Anti-aligned)	2 (Aligned)
2	2.5 (Aligned)	2 (Aligned)
3	2.5 (Aligned)	3 (Anti-aligned)
4	3.5 (Anti-aligned)	2 (Aligned)
5	3.5 (Anti-aligned)	3 (Anti-aligned)

SUMMARY

Five double pyridazine molecular rotors differing in inter- and intramolecular pyridazine-pyridazine spacing were synthesized and included as guests in the TPP host to obtain bulk inclusion compounds. Their formation was confirmed using solid-state NMR and powder X-ray diffraction. It was proven that the absence of triple bond carbon resonances located next to the BCP cage is due to inefficient cross-polarization in the spectra of inclusion compounds and could be used as an additional proof of inclusion. The rotation of pyridazine rotators was independently studied by dielectric spectroscopy and solid-state NMR. Dielectric spectroscopy results are well described by a simple model where the pyridazine dipole moments move in local three-fold rotational potentials. Interestingly, neighboring dipoles can occupy two different types of correlated three-fold potentials depending upon the separation of neighbors: For dipoles located approximately an even number of TPP layers apart, the three-fold potentials are identical and therefore have wells that are at identical dipole orientations. Dipoles located an odd number of layers apart experience three-fold potentials that are rotated by 180°, allowing for anti-aligned dipole orientations. The data sets are well fitted by two different 9-state model susceptibilities, with dipole-dipole interactions of 100 to 200 K in rough agreement with those predicted for these two distinct types of system, and which lead to different energies and equilibrium population differences that match the dielectric susceptibilities observed in the various inclusion compounds. The

pyridazines substituted by ethynyl units in both 3- and 6- positions have a slightly higher rotational barrier (3.2 - 3.5 kcal/mol) than those carrying one ethynyl and one *tert.*-Bu group (1.9 - 3.0 kcal/mol). These values seem to be still too high for achieving a ferroelectric ground state. Calculations of rotational barriers for **1**@TPP (<4.5 kcal/mol) reveal the expected three-fold approximate symmetry and correlate reasonably with experimentally obtained value (2.5 kcal/mol).

Overall, these results indicate that our understanding of these inclusion systems is reaching the point where fairly simple design rules can be followed to synthesize pyridazine-based rotor molecules with low rotation barriers and where the remaining potential landscape within the TPP channels might be used to enforce a preference for ferroelectric alignments.

EXPERIMENTAL SECTION

Materials. All reactions were carried out under argon atmosphere with dry solvents freshly distilled under anhydrous conditions. Standard Schlenk and vacuum line techniques were employed for all manipulations of air- or moisture-sensitive compounds. Yields refer to isolated, chromatographically and spectroscopically homogenous materials.

1,3-Diethynylbicyclo[1.1.1]pentane (**17**),[37,38] 1,3-bis((trimethylsilyl)ethynyl)bicyclo-[1.1.1]pentane (**16**),[37,38] and TPP-d_{12}[18] were synthesized according to published procedures. THF and ether were dried over sodium with benzophenone and distilled under argon prior to use. Triethylamine and CH_2Cl_2 were dried over CaH_2 and distilled under argon prior to use. All other reagents were used as supplied unless otherwise stated.

The code for designating an inclusion compound is X%Y@TPP-d_{12}, where X is the molar percentage of rotor Y.

The published procedure[19] for preparing the inclusion compounds from components was modified as follows. The neat rotors **1** - **5** (amounts of guest used for preparation of inclusion compounds are in Table S2), and neat solvent-free hexagonal TPP-d_{12} (100 mg, 0.212 mmol) were mixed, and ball milled five times in 5 min. intervals at room temperature using stainless steel ball mill. Between each of those periods, the sample was thoroughly scratched from the walls. Finally, the white fine powders were recovered and placed into a small vial wrapped in the aluminum foil. This vial was inserted into a small flask and aubjected to three vacuum/argon cycles. The flask was then tightly closed and annealed under argon for 24 hours at 70 °C.

Procedures. Analytical thin-layer chromatography (TLC) was performed using precoated TLC aluminum sheets (Silica gel 60 F_{254}). TLC spots were visualized using either UV light (254 nm) or a 5% solution of phosphomolybdic acid in ethanol, and heat (200 °C) as a developing agent. Flash chromatography was performed using silica gel (high purity grade, pore size 60 Å, 70 - 230 mesh). Melting points are reported uncorrected. Chemical shifts in ^{1}H, and ^{13}C spectra are reported in ppm on the δ scale relative to $CHCl_3$ (δ = 7.26 ppm for ^{1}H and δ = 77.0 ppm for ^{13}C), acetone-d_6 (δ = 2.05 ppm for ^{1}H, and δ = 29.8 and 206.3 ppm for ^{13}C), THF-d_8 (δ = 1.72 and 3.58 ppm for ^{1}H, and δ = 25.40 and 67.50 ppm for ^{13}C), as internal references. The volume/volume (v/v) ratios of solvents were used to prepare mobile phases for column chromatographies.

High-resolution mass spectra (HRMS) using atmospheric-pressure chemical ionization (APCI) and electrospray ionization (ESI) were obtained on a mass analyzer combining linear ion trap and the Orbitrap, and those using chemical ionization (CI) mode were taken on a time-of-flight mass spectrometer. Assignment of the ions in the mass spectra was based on simulation of the isotope envelopes using software provided by the manufacturer of mass spetrometers.

X-Ray Diffraction. Crystallographic data were collected either on Nonius Kappa CCD diffractometer (compounds **9**, **19**, and **21**) equipped with Bruker APEX-II CCD detector by monochromatized MoKα radiation (λ = 0.71073 Å) or on Bruker D8 VENTURE Kappa Duo PHOTON100 (compounds **1**, **2**, and **18**) by IμS micro-focus sealed tube CuKα (λ = 1.54178 Å) at a temperature of 150(2) K. The structures were solved by direct methods (XP)[58] and refined by full matrix least squares based on F^2 (SHELXL2014).[59] The hydrogen atoms on carbon were fixed into idealized positions (riding model) and assigned temperature factors either $H_{iso}(H) = 1.2\ U_{eq}$ (pivot atom) or $H_{iso}(H) = 1.5\ U_{eq}$ (pivot atom) for methyl moiety.

Powder X-ray Diffraction. The X-ray powder patterns were taken using two different systems: (i) Bruker D8 Discoverer powder diffractometer using Cu Kα radiation at a wavelength of λ = 0.15418 nm and line detector LYNXEYE XE. Powder samples were loaded on silicon holder (6° off cut from (111)). The measurement was performed in the range of 5 - 80° 2θ with a step 0.02° 2θ and 1 s/step measurement time. Powder samples, loaded into 1.0 mm diameter borosilicate glass capillaries with a wall thickness of 10 μm, were mounted on a Huber four-circle goniometer. The scattered X-rays were measured with a NaI scintillator point detector that was moved in a horizontal plane by an angle 2θ with respect to the direction of the incident X-rays to scan the Bragg scattering profile. The resolution of the instrument, in its usual configuration, is $q_{res} \approx 0.003$ Å^{-1}. (ii) Diffractometer based on a Rigaku MiniFlex 600 using Cu Kα radiation at an average wavelength of λ = 0.15418 nm, and a D/Tex Ultra 1D silicon strip detector. Powder samples were loaded into single-crystal quartz substrates, which were cut to prevent unwanted quartz diffraction peaks.

Transmission Electron Microscopy. The sample was prepared by dropping an aqueous suspension of 30%**1**@TPP-d_{12} onto a carbon-coated copper grid and drying in air. Images were recorded with a JEOL JEM-1011 transmission electron microscope operated at 60 kV.

DSC Analysis was performed on a DSC Q20 (TA Instruments). Analysis of all samples (neat **1** - **5**, TPP-d_{12}, and unsaturated and saturated bulk inclusion compounds) consisted of three parts at 10 ℃/min. The first part was heating from room temperature to 310 ℃, the second was cooling to 40 ℃, and the third was warming to 310 ℃. Standard loading was 4.0 - 7.5 mg.

Dielectric Spectroscopy. The powder samples were loaded onto the surface of coplanar interdigitated electrode capacitators fabricated by gold metallization on fused silica substrates (each with 50 fingers separated by ~10 μm gaps). Nominal capacitor values for the empty capacitors were near 1 pF and dielectric loss tangents were at or below 10^{-5} level. An Andeen-Hagerling capacitance bridge was used to measure the dielectric loss and capacitance with sinusoidal alternating voltage (1.8 - 5 V and 0.10 - 20 kHz) applied on the capacitor. Data were taken continuously with the temperature slowly changing between 7 K and room temperature.

Calculations. The guest molecule **1** was included in a four-layer model of the TPP lattice, with one **1** in each of its seven channels. The optimal positions of all guests in the lattice were optimized at the MP6-D3H4[60] level with the whole lattice fully relaxed in the first step. The resulting structure had only approximately a threefold symmetry, because the centrally located **1** itself has a lower symmetry. To achieve the threefold symmetry expected for the time-averaged potential, the pyridazine in the rotor molecule located in the central channel was replaced with a non-polar 1,2,4,5-tetrazine and the TPP lattice was averaged over the 16 symmetry-related models shown in Figure S9. Then the six channels surrounding the central channel were fixed to reduce the effects of truncation of the solid in the simulation

of the rotational barrier of **1** (Figure S8 in Supporting Information). The dihedral angles φ_1 and φ_2 of the two pyridazine rings of **1** were fixed in steps of 15° and the remainder of the central TPP channel was fully relaxed to locate the optimal conformation of **1**. The rotational potential was calculated at the B97-D3/SVP[35] level as a function of φ_1 and φ_2. The simulations were performed with the programs MOPAC2016[61] and TURBOMOLE V7.2.[62]

The NMR shieldings of **1** were calculated by the CASTEP program,[63] version 8.0, which is a DFT-based code that uses pseudopotentials to model the effects of core electrons, and plane waves to describe the valence electrons. Positions of all atoms were optimized prior to the NMR calculation; the unit cell parameters were fixed. Electron-correlation effects were modeled using the generalized gradient approximation of Perdew, Burke, and Ernzerhof.[64] A plane wave basis set energy cutoff of 600 eV, default "on the fly generation" pseudopotentials, and a *k*-point spacing of 0.05 $Å^{-1}$ over the Brillouin zone via a Monkhorst-Pack grid[65] was used. The NMR calculations were performed using the GIPAW approach.[66,67]

Solid-State NMR. High-resolution ^{13}C and ^{31}P solid-state NMR spectra were obtained using a Bruker Avance II spectrometer operating at 125.7 MHz for ^{13}C, 202.4 MHz for ^{31}P, and 499.9 MHz for ^{1}H. Samples were packed into 3.2 mm magic angle spinning (MAS) rotors and measurements taken using a MAS rate of 4-20 kHz using cross polarization or direct excitation. The typical CP conditions used were: recycle delay 4 s, contact time 2 ms, acquisition time 30 ms. The ^{13}C spectra were referenced with respect to external neat tetramethylsilane by setting the carbonyl signal from a replacement sample of α-glycine to 176.03 ppm. Phosphorus spectra were referenced against $(NH_4)_2HPO_4$ (δ = 1.37 ppm). The assignment of the ^{13}C SS-NMR signals was based on comparison with solution-state spectrum, DFT calculated chemical shifts (see Calculations section for more details), and short CP-MAS experiment (with the contact time of 40 μs), where only signals of carbon atoms directly attached to a hydrogen are observable.

Synthesis. 1,2-Bis(6-*tert*-butylpyridazin-3-yl)ethyne (1). A flame-dried Schlenk flask was charged with alkyne **11** (250 mg, 1.560 mmol, 1.0 equiv.), **9** (491 mg, 1.872 mmol, 1.2 equiv.), $Pd(PPh_3)_4$ (72 mg, 0.062 mmol, 4 mol %), and CuI (9 mg, 0.047 mmol, 3 mol %). After three successive vacuum/argon cycles, degassed dry THF (10 mL) and triethylamine (5 mL) were added from a syringe. The slightly yellowish solution was stirred for 18 h at room temperature. A dense white solid precipitated. The crude reaction mixture was diluted with CH_2Cl_2 (150 mL) and washed with saturated aqueous NH_4Cl (2 × 30 mL). A clear yellowish organic phase was dried over $MgSO_4$ and volatiles were removed under reduced pressure. Column chromatography on silica gel (hexane/EtOAc - 1:1 to remove unreacted starting materials followed by hexane/EtOAc/CH_2Cl_2 - 1:1:1 to elute product) provided **1** as a white crystalline solid (415 mg, 1.410 mmol, 90%).

Mp 246.4 - 247.9 °C. ^{1}H NMR (400 MHz, $CDCl_3$): δ 1.47 (s, 9H), 7.54 (d, J = 8.84 Hz, 2H), 7.68 (d, J = 8.83 Hz, 2H). ^{13}C {^{1}H} NMR (100 MHz, $CDCl_3$): δ 29.9, 37.2, 88.8, 122.5, 130.0, 144.9, 169.2. IR (KBr): 3078, 3050, 2968, 2931, 2903, 2869, 2126, 1582, 1539, 1475, 1462, 1425, 1370, 1365, 1336, 1299, 1271, 1202, 1163, 1151, 1078, 944, 930, 867, 694, 508 cm^{-1}. MS (EI), *m/z* (%): 294.2 (22, M), 279.2 (57, M - CH_3), 252.1 (100), 237.1 (10, M – *t*-Bu), 210.1 (18). HRMS (EI) (*m/z*): $[M]^+$ Calcd for $C_{18}H_{22}N_4^+$, 294.1844; found, 294.1843. Anal. Calcd. for $C_{18}H_{22}N_4$: C, 73.44; H, 7.53; N, 19.03. Found: C, 73.24; H, 7.53; N, 18.73.

1,3-Bis((6-*tert*-butylpyridazin-3-yl)ethynyl)bicyclo[1.1.1]pentane (**2**). A flame-dried Schlenk flask was charged with **16**[35] (300 mg, 1.152 mmol), **9** (755 mg, 2.880 mmol, 2.5 equiv.), $Pd(PPh_3)_4$ (53 mg, 0.046 mmol, 4 mol %), and CuI (7 mg, 0.035 mmol, 3 mol %). After three successive vacuum/argon cycles, dry and degassed THF (8 mL) and triethylamine (10 mL) were added from a syringe. Subsequently, solution of TBAF in THF (1.0 M, 2.42 mL, 2.419 mmol, 2.1 equiv.) was added to the reaction mixture. The yellow solution was stirred in an oil bath for 18 h at 40 °C. A dense white solid precipitated. The crude reaction mixture was diluted with CH_2Cl_2 (150 mL), washed with saturated aqueous NH_4Cl (2 × 40 mL) and dried over $MgSO_4$. Column chromatography on silica gel (hexane/EtOAc - 1:1 to elute impurities and hexane/EtOAc/CH_2Cl_2 - 1:1:1 to elute product) provided a brownish solid, which was subsequently triturated with EtOAc (8 × 1 mL). Compound **2** was obtained as a white crystalline solid (362 mg, 0.941 mmol, 82%).

Mp > 250 °C (dec.). ^{1}H NMR (400 MHz, $CDCl_3$): δ 1.42 (s, 18H), 2.56 (s, 6H), 7.40 - 7.44 (m, 4H). ^{13}C {^{1}H} NMR (100 MHz, $CDCl_3$): δ 29.9, 30.7, 37.0, 58.9, 77.3, 91.6, 122.2, 129.4, 145.4, 168.4. IR (KBr): 3042, 2959, 2916, 2877, 2236, 2217, 1578, 1536, 1473, 1461, 1420, 1366, 1329, 1301, 1272, 1203, 1148, 1105, 1047, 850, 803, 690, 531 cm^{-1}. MS (APCI), *m/z* (%): 385.2 (100, M + H). HRMS (APCI) (*m/z*): $[M + H]^+$ Calcd for $C_{25}H_{29}N_4^+$, 385.2387; found, 385.2387. Anal. Calcd. for $C_{25}H_{28}N_4$: C, 78.09; H, 7.34; N, 14.57. Found: C, 77.98; H, 7.32; N, 14.40.

1,3-Bis((6-(3,3-dimethylbut-1-ynyl)pyridazin-3-yl)ethynyl)bicyclo[1.1.1]pentane (**3**). A flame-dried Schlenk flask was charged with **16**[37] (350 mg, 1.343 mmol), **12** (845 mg, 2.955 mmol, 2.2 equiv.), $Pd(PPh_3)_4$ (62 mg, 0.054 mmol, 4 mol %), and CuI (8 mg, 0.040 mmol, 3 mol %). After three successive vacuum/argon cycles, dry and degassed THF (8 mL) and triethylamine (10 mL) were added from a syringe. Subsequently, solution of TBAF in THF (1.0 M, 2.82 mL, 2.820 mmol, 2.1 equiv.) was added to the reaction mixture. The yellow solution was stirred in an oil bath for 18 h at 40 °C. A dense white solid precipitated. The crude reaction mixture was diluted with CH_2Cl_2 (150 mL), washed with saturated aqueous NH_4Cl (2 × 40 mL) and dried over $MgSO_4$. Column chromatography on silica gel (EtOAc/CH_2Cl_2 - 1:1) provided a brownish solid, which was subsequently washed on frit with methanol (4 × 2 mL), and EtOAc (4 × 2 mL). Compound **3** was obtained as a white crystalline solid (425 mg, 0.983 mmol, 73%).

Mp > 260 °C (dec.). ^{1}H NMR (400 MHz, $CDCl_3$): δ 1.36 (s, 18H), 2.57 (s, 6H), 7.41 (s, 4H). ^{13}C {^{1}H} NMR (100 MHz, $CDCl_3$): δ 28.2, 30.5, 30.8, 58.9, 76.4, 77.2, 93.6, 105.6, 128.7, 128.8, 145.1, 146.3. IR (KBr): 3108, 3072, 3042, 2968, 2924, 2900, 2879, 2238, 1568, 1526, 1475, 1457, 1396, 1364, 1327, 1295, 1277, 1204, 1120, 1104, 1059, 1033, 919, 869, 820, 662 cm^{-1}. MS (APCI), *m/z* (%): 433.2 (100, M + H). HRMS (APCI) (*m/z*): $[M + H]^+$ Calcd for $C_{29}H_{29}N_4^+$, 433.2387; found, 433.2387. Anal. Calcd. for $C_{29}H_{28}N_4$: C, 80.52; H, 6.52; N, 12.95. Found: C, 80.39; H, 6.44; N, 12.85.

1,3-Bis((6-*tert*-butylpyridazin-3-yl)buta-1,3-diynyl)bicyclo[1.1.1]pentane (**4**). *Warning: This compound is explosive and detonates spontaneously at temperatures above 200 °C. It should be handled with caution!* A flame-dried Schlenk flask was charged with **9** (472 mg, 1.800 mmol, 3.0 equiv.), $Pd(PPh_3)_4$ (28 mg, 0.024 mmol, 4 mol %), and CuI (3 mg, 0.018 mmol, 3 mol %). After three successive vacuum/argon cycles, a solution of tetrayne **18** (98 mg, 0.600 mmol) in dry and degassed THF (6 mL) followed by triethylamine (5 mL) was added from a syringe. The slightly yellowish solution was stirred for 18 h at room temperature. A dense white solid precipitated. The crude reaction mixture was diluted with

CH_2Cl_2 (100 mL), washed with saturated aqueous NH_4Cl (2 × 20 mL) and dried over $MgSO_4$. Column chromatography on silica gel (EtOAc/CH_2Cl_2 - 1:1) gave a brownish solid, which was subsequently washed on frit with methanol (3 × 5 mL), and EtOAc (3 × 5 mL). Compound **4** was obtained as a white crystalline solid (136 mg, 0.314 mmol, 52%).

Mp > 200 °C (dec.). ^{1}H NMR (500 MHz, $CDCl_3$): δ 1.44 (s, 18H), 2.48 (s, 6H), 7.44 - 7.49 (m, 4H). ^{13}C {^{1}H} NMR (125 MHz, $CDCl_3$): δ 29.8, 30.6, 37.2, 59.2, 64.5, 73.0, 77.03, 83.1, 122.2, 130.4, 144.8, 168.8. IR (KBr): 3034, 2968, 2954, 2921, 2882, 2234, 1572, 1533, 1474, 1458, 1411, 1363, 1359, 1228, 1153, 1125, 1098, 1025, 860, 845, 787, 771, 764, 736 cm^{-1}. MS (APCI), *m/z* (%): 433.2 (100, M + H). HRMS (APCI) (*m*/*z*): [M + H]$^+$ Calcd for $C_{29}H_{29}N_4^+$, 433.2387; found, 433.2387. Anal. Calcd. for $C_{29}H_{28}N_4$: C, 80.52; H, 6.52; N, 12.95. Found: C, 80.49; H, 6.35; N, 12.85.

1,3-Bis((6-(3,3-dimethylbut-1-ynyl)pyridazin-3-yl)buta-1,3-diynyl)bicyclo[1.1.1]pentane (**5**). *Warning: This compound is explosive and detonates spontaneously at temperatures above 200 °C. It should be handled with caution!* A flame-dried Schlenk flask was charged with **12** (654 mg, 2.286 mmol, 2.5 equiv.), $Pd(PPh_3)_4$ (42 mg, 0.037 mmol, 4 mol %), and CuI (5 mg, 0.027 mmol, 3 mol %). After three successive vacuum/argon cycles, a freshly purified tetrayne **18** (150 mg, 0.914 mmol) was added in a stream of argon. Subsequently, dry and degassed THF (10 mL) followed by triethylamine (10 mL) were added from a syringe. A dense white solid precipitated immediately, and this suspension was stirred for 18 h at room temperature. Solids were filtered on a frit and thoroughly washed with water (30 mL), methanol (3 × 15 mL), and EtOAc (3 × 10 mL). Compound **5** was obtained as a white crystalline solid (300 mg, 0.624 mmol, 68%).

Mp 248 °C (explosion!). ^{1}H NMR (500 MHz, $CDCl_3$): δ 1.36 (s, 18H), 2.48 (s, 6H), 7.40 - 7.47 (m, 4H). ^{13}C {^{1}H} NMR (125 MHz, $CDCl_3$): δ 28.3, 30.4, 30.6, 59.2, 64.4, 72.7, 76.4, 79.1, 84.3, 106.4, 128.5, 129.5, 144.5, 146.4. IR (KBr): 3069, 3021, 3003, 2969, 2922, 2899, 2867, 2232, 1569, 1528, 1475, 1456, 1402, 1363, 1345, 1309, 1281, 1231, 1203, 1156, 1116, 1096, 1036, 917, 866, 845, 805, 772, 728, 663, 625, 545 cm^{-1}. MS (APCI), *m/z* (%): 481.2 (100, M + H). HRMS (APCI) (*m*/*z*): [M + H]$^+$ Calcd for $C_{33}H_{29}N_4^+$, 481.2387; found, 481.2387. Anal. Calcd. for $C_{33}H_{28}N_4$: C, 82.47; H, 5.87; N, 11.66. Found: C, 82.56; H, 5.86; N, 11.42.

6-*tert*-Butylpyridazin-3(*2H*)-one (**7**). A published procedure[36] was adapted as follows: A stirred suspension of glyoxylic acid monohydrate (9.205 g, 100.000 mmol, 1.0 equiv.) in 3,3-dimethylbutan-2-one (37.51 mL, 300.000 mmol, 3.0 equiv.) was heated in an oil bath at 100 - 105 °C for 2 h (suspension dissolved leaving clear yellowish solution). The reaction mixture was then cooled to 20 °C, distilled water (20 mL) was added and the pH of the solution was adjusted to ca 8 using saturated aqueous NH_3. The organic phase was removed and a clear orange water phase was washed with CH_2Cl_2 (3 × 50 mL). Unreacted starting 3,3-dimethylbutan-2-one was then recovered from this organic phase. Clear orange aqueous phase was then treated with hydrazine monohydrate (4.85 mL, 100.000 mmol, 1.0 equiv.) and the mixture was refluxed for additional 2 h. Cooling of the solution to room temperature caused crystallization of white material, which was filtered on frit, washed with water (2 × 30 mL) and thoroughly dried under reduced pressure. Compound **7** was isolated as a white crystalline solid (2.039 g, 13.398 mmol, 13%).

Mp 163.8 - 165.2 °C. ^{1}H NMR (400 MHz, Acetone-d_6): δ 1.27 (s, 9H), 6.84 (dd, J_1 = 0.49 Hz, J_2 = 9.93 Hz, 1H), 7.60 (d, J = 9.93 Hz, 1H), 12.16 (br s, 1H). ^{13}C {^{1}H} NMR (100 MHz, Acetone-d_6): δ 29.2, 36.5, 130.6, 132.3, 154.9, 161.2. IR (KBr): 3207, 3159,

3131, 3055, 3002, 2971, 2871, 1686, 1652, 1597, 1549, 1534, 1475, 1449, 1411, 1398, 1308, 1284, 1202, 1143, 1138, 1121, 1028, 1007, 940, 926, 851, 836, 767, 685, 630, 588, 522, 514 cm^{-1}. MS (EI), *m/z* (%): 152.1 (37, M), 137.1 (100, M - CH_3), 110 (22). HRMS (EI) (*m/z*): $[M]^+$ Calcd for $C_8H_{12}N_2O^+$, 152.0950; found, 152.0949. Anal. Calcd. for $C_8H_{12}N_2O$: C, 63.13; H, 7.95; N, 18.41. Found: C, 63.20; H, 7.80; N, 18.43.

3-*tert*-Butyl-6-chloropyridazine (**8**). Suspension of **7** (3.000 g, 19.712 mmol) in $POCl_3$ (15.00 mL, 160.927 mmol) was stirred in an oil bath at 100 °C for 2 h. Solid material slowly dissolved leaving clear brownish solution. Volatiles were then distilled off under reduced pressure, brownish oily residue was dissolved in CH_2Cl_2 (100 mL) and washed with an ice-cold 70% aqueous NaOH (100 mL). The aqueous phase was extracted with CH_2Cl_2 (2 × 50 mL) and combined organic phases were dried over $MgSO_4$. Column chromatography on silica gel (hexane/EtOAc - 3:2) yielded **8** as a white crystalline solid (3.093 g, 18.126 mmol, 92%).

Mp 90.5 - 91.6 °C. ^1H NMR (400 MHz, $CDCl_3$): δ 1.42 (s, 9H), 7.41 (d, *J* = 8.99 Hz, 1H), 7.49 (d, *J* = 8.99 Hz, 1H). ^{13}C {^1H} NMR (100 MHz, $CDCl_3$): δ 29.9, 36.8, 125.8, 127.9, 154.7, 169.5. IR (KBr): 3036, 2980, 2966, 2930, 2904, 2867, 1569, 1536, 1480, 1472, 1463, 1412, 1369, 1364, 1321, 1273, 1202, 1178, 1135, 1039, 1033, 940, 928, 855, 842, 770, 599 cm^{-1}. MS (EI), *m/z* (%): 169.1 (20, M), 155.0 (100, M - CH_3), 128.0 (68). HRMS (EI) (*m/z*): $[M]^+$ Calcd for $C_8H_{11}ClN_2^+$, 170.0611; found, 170.0610. Anal. Calcd. for $C_8H_{11}ClN_2$: C, 56.31; H, 6.50; N, 16.42. Found: C, 56.30; H, 6.49; N, 16.35.

3-*tert*-Butyl-6-iodopyridazine (**9**). A solution of 3-*tert*-butyl-6-chloropyridazine (**8**) (2.500 g, 14.651 mmol) and NaI (3.074 g, 20.511 mmol, 1.4 equiv.) in 57% aqueous HI (25 mL) was stirred in an oil bath 30 min at 70 °C and 3 h at 100 °C. A dense yellow precipitate was formed. The reaction mixture was cooled to room temperature and then carefully poured into the ice-cold 70% aqueous NaOH (100 mL). The aqueous phase was extracted with CH_2Cl_2 (3 × 50 mL) and a slightly yellowish combined organic phase was dried over $MgSO_4$. Solvent was removed under reduced pressure and column chromatography on silica gel (hexane/ethyl-acetate, 3:2) yielded **9** as a white crystalline solid (3.658 g, 13.957 mmol, 95%).

Mp 112.2 - 113.6 °C. ^1H NMR (400 MHz, $CDCl_3$): δ 1.40 (s, 9H), 7.19 (d, *J* = 8.91 Hz, 1H), 7.75 (d, *J* = 8.91 Hz, 1H). ^{13}C {^1H} NMR (100 MHz, $CDCl_3$): δ 29.7, 36.9, 122.8, 124.7, 136.9, 169.5. IR (KBr): 3116, 3090, 3063, 3030, 2967, 2903, 2867, 1559, 1522, 1476, 1462, 1402, 1364, 1311, 1272, 1202, 1182, 1165, 1147, 1112, 1037, 1012, 940, 927, 853, 841, 768, 748, 632, 569 cm^{-1}. MS (EI), *m/z* (%): 262.0 (12, M), 247.0 (82, M - CH_3), 220.0 (100), 126.9 (17, I). HRMS (EI) (*m/z*): $[M]^+$ Calcd for $C_8H_{11}IN_2^+$, 261.9967; found, 261.9966. Anal. Calcd. for $C_8H_{11}IN_2$: C, 36.66; H, 4.23; N, 10.69. Found: C, 37.03; H, 4.28; N, 10.69.

3-*tert*-Butyl-6-((trimethylsilyl)ethynyl)pyridazine (**10**). A flame-dried Schlenk flask was charged with **9** (600 mg, 2.289 mmol, 1.0 equiv.), $Pd(PPh_3)_4$ (106 mg; 0.092 mmol, 4 mol %), and CuI (13 mg, 0.069 mmol, 3 mol %). After three successive vacuum/argon cycles, TMSA (485 µL, 3.434 mmol, 1.5 equiv.), degassed dry THF (10 mL) and triethylamine (5 mL) were added from a syringe. The slightly yellowish solution was stirred for 18 h at room temperature. A dense white solid precipitated. The crude reaction mixture was diluted with ether (150 mL) and washed with saturated aqueous NH_4Cl (2 × 40 mL). A clear yellowish organic phase was dried over $MgSO_4$ and volatiles were removed under

reduced pressure. Column chromatography on silica gel (hexane/EtOAc - 4:1) provided **10** as a white crystalline solid (488 mg, 2.100 mmol, 92%).

Mp 130.1 - 131.7 °C. ^{1}H NMR (400 MHz, $CDCl_3$): δ 0.28 (s, 9H), 1.43 (s, 9H), 7.42 - 7.47 (m, 2H). ^{13}C {^{1}H} NMR (100 MHz, $CDCl_3$): δ -0.4, 29.8, 37.0, 99.1, 101.0, 122.2, 129.6, 145.4, 168.5. IR (KBr): 3120, 3079, 3045, 2962, 2905, 2870, 2172, 1576, 1539, 1477, 1464, 1411, 1369, 1323, 1264, 1252, 1148, 1075, 871, 845, 763, 711, 654, 626, 539 cm^{-1}. MS (CI), *m/z* (%): 233.1 (100, M + H), 217.1 (35, M - CH_3), 190.1 (30). HRMS (CI) (*m/z*): $[M + H]^+$ Calcd for $C_{13}H_{21}N_2Si^+$, 233.1474; found, 233.1473. Anal. Calcd. for $C_{13}H_{20}N_2Si$: C, 67.19; H, 8.67; N, 12.09. Found: C, 67.36; H, 8.52; N, 11.76.

3-*tert*-Butyl-6-ethynylpyridazine (**11**). To a stirred solution of **10** (440 mg, 1.893 mmol, 1.0 equiv) in wet THF (10 mL), a solution of TBAF in THF (1.0 M, 2.27 mL, 2.272 mmol, 1.2 equiv.) was added at room temperature. The reddish reaction mixture was stirred for 30 min, diluted with ether (80 mL), washed with water (2 × 20 mL), and the clear yellowish organic phase was dried over $MgSO_4$. Solvents were removed under reduced pressure and column chromatography on silica gel (hexane/EtOAc - 4:1) gave alkyne **11** as a white crystalline solid (298 mg, 1.860 mmol, 98%).

Mp 73.8 - 74.1 °C. ^{1}H NMR (400 MHz, $CDCl_3$): δ 1.44 (s, 9H), 3.34 (s, 1H), 7.46 - 7.52 (m, 2H). ^{13}C {^{1}H} NMR (100 MHz, $CDCl_3$): δ 29.9, 37.1, 80.3, 80.8, 122.3, 129.8, 144.8, 169.0. IR (KBr): 3271, 3077, 3045, 2966, 2930, 2903, 2869, 2117, 1579, 1536, 1477, 1466, 1447, 1414, 1369, 1323, 1277, 1234, 1203, 1163, 1149, 1070, 942, 866, 846, 798, 789, 703, 664, 655, 530 cm^{-1}. MS (CI), *m/z* (%): 161.1 (100, M + H), 145.1 (12, M - CH_3), 118.1 (18). HRMS (CI) (*m/z*): $[M + H]^+$ Calcd for $C_{10}H_{13}N_2^+$, 161.1079; found, 161.1077. Anal. Calcd. for $C_{10}H_{12}N_2$: C, 74.97; H, 7.55; N, 17.48. Found: C, 74.82; H, 7.55; N, 17.08.

3-(3,3-Dimethylbut-1-ynyl)-6-iodopyridazine (**12**). A flame-dried Schlenk flask was charged with **14** (4.646 g, 14.000 mmol, 1.0 equiv.), $Pd(PPh_3)_4$ (647 mg, 0.560 mmol, 4 mol %), and CuI (80 mg, 0.420 mmol, 3 mol %). After three successive vacuum/argon cycles, degassed dry THF (40 mL) and triethylamine (10 mL) were added from a syringe. Subsequently, 3,3-dimethylbut-1-yne (1.72 mL, 14.000 mmol, 1.0 equiv.) was added from a syringe. The slightly yellowish solution was stirred in an oil bath for 18 h at 70 °C. Reaction mixture turned black and a dense white solid precipitated. The crude reaction mixture was cooled to room temperature, diluted with ether (150 mL), and washed with saturated aqueous NH_4Cl (3 × 30 mL). A black organic phase was dried over $MgSO_4$ and volatiles were removed under reduced pressure. Two runs of column chromatography on silica gel (hexane/EtOAc - 5:1) provided **12** as a white crystalline solid (1.690 g, 5.907 mmol, 42%).

Mp 89.0 - 90.8 °C (dec.). ^{1}H NMR (400 MHz, $CDCl_3$): δ 1.35 (s, 9H), 7.13 (d, J = 8.73 Hz, 1H), 7.76 (d, J = 8.73 Hz, 1H). ^{13}C {^{1}H} NMR (100 MHz, $CDCl_3$): δ 28.2, 30.4, 75.6, 105.7, 122.3, 130.3, 136.2, 147.7. IR (KBr): 3088, 3055, 2969, 2929, 2901, 2866, 2240, 2210, 1554, 1524, 1507, 1474, 1457, 1385, 1363, 1305, 1290, 1269, 1203, 1137, 1103, 1050, 1024, 914, 858, 797, 703, 638 cm^{-1}. MS (EI), *m/z* (%): 286.0 (100, M), 271.0 (25, M - CH_3), 126.9 (18), 115.1 (14), 91.1 (10). HRMS (EI) (*m/z*): $[M]^+$ Calcd for $C_{10}H_{11}IN_2^+$, 285.9967; found, 285.9974. Anal. Calcd. for $C_{10}H_{11}IN_2$: C, 41.98; H, 3.88; N, 9.79. Found: C, 42.04; H, 4.13; N, 9.70.

1,3-Di(buta-1,3-diynyl)bicyclo[1.1.1]pentane (**18**). *Warning: This compound is highly explosive and should be handled with a great caution and only by trained personnel! It is strongly recommended to store it as an ethereal or THF solution. When dry it spontaneously*

detonates at temperatures above 80 °C. The solution of *n*-BuLi in hexane (2.5 M, 4.61 mL, 11.533 mmol, 6.0 equiv.) was added dropwise to a solution of **21** (930 mg, 1.922 mmol) in ether (50 mL) cooled at -78 °C. A light grayish precipitate was formed immediately. The suspension was stirred at -78 °C for 3 h. Subsequently, saturated aqueous NH_4Cl (10 mL) was added, cooling was stopped and the solution was allowed to heat to room temperature. The reaction mixture was diluted with ether (20 mL) and washed with saturated aqueous NH_4Cl (2 × 20 mL). The clear yellowish organic phase was dried over $MgSO_4$ and volatiles were carefully removed under slightly reduced pressure (550 Torr) in a water bath kept at 45 °C. Column chromatography on silica gel (pentane) gave **18** as a white crystalline solid with characteristic acetylene odor (259 mg, 1.579 mmol, 82%).

Mp 85 °C (explosion!). ^{1}H NMR (400 MHz, $CDCl_3$): δ 2.06 (s, 2H), 2.37 (s, 6H). ^{13}C {^{1}H} NMR (100 MHz, $CDCl_3$): δ 30.1, 58.9, 64.6, 66.7, 67.7, 74.7. IR (KBr): 3282, 2999, 2969, 2917, 2880, 2259, 2234, 2213, 2061, 1449, 1251, 1169, 1120, 922, 880, 798, 639, 625 cm^{-1}. MS (CI), *m/z* (%): 165.1 (34, M + H), 164.1 (100, M), 139.1 (48, M - CCH), 115.1 (55, M - CC-CCH). HRMS (CI) (*m/z*): $[M]^+$ Calcd for $C_{13}H_8^+$, 164.0626; found, 164.0627. Anal. Calcd. for $C_{13}H_8$: C, 95.09; H, 4.91. Found: C, 95.19; H, 4.63.

3,3'-(Bicyclo[1.1.1]pentane-1,3-diyl)diprop-2-yn-1-ol (**19**). To the solution of freshly sublimed diyne **17**[35,36] (800 mg, 6.887 mmol) in THF (20 mL) at -78 °C was dropwise added *n*-BuLi in hexane (1.6 M, 10.76 mL, 17.218 mmol, 2.5 equiv.). A dense white precipitate was formed immediately. The white suspension was stirred for 30 min at -78 °C. Subsequently, dry solid paraformaldehyde (620 mg, 20.661 mmol, 3.0 equiv.) was added and the suspension was stirred for additional 20 min at the same temperature. Cooling was stopped and the reaction mixture was slowly warmed to room temperature and stirred for 60 min. The reaction was quenched with saturated aqueous NH_4Cl (5 mL) and the solution was stirred for additional 30 min. The reaction mixture was diluted with diethyl ether (150 mL), washed with saturated aqueous NH_4Cl (2 × 30 mL), and the clear yellow organic phase was dried over $MgSO_4$. Volatiles were removed under reduced pressure. Column chromatography on silica gel (hexane/acetone - 4:3) provided **19** (846 mg, 4.801 mmol, 70%) as a white crystalline solid.

Mp 149.4 - 150.0 °C. ^{1}H NMR (400 MHz, $CDCl_3$): δ 1.61 (br s, 2H), 2.29 (s, 6H), 4.24 (s, 4H). ^{13}C {^{1}H} NMR (100 MHz, $CDCl_3$): δ 30.0, 51.2, 58.5, 78.2, 84.4. IR (KBr): 3256, 2990, 2967, 2914, 2876, 2248, 2218, 1505, 1488, 1448, 1356, 1323, 1256, 1234, 1161, 1014, 984, 965, 886, 792, 609 cm^{-1}. MS (APCI), *m/z* (%): 177.1 (25, M + H), 159.1 (100, M - OH). HRMS (APCI) (*m/z*): $[M + H]^+$ Calcd for $C_{11}H_{13}O_2^+$, 177.0910; found, 177.0911. Anal. Calcd. for $C_{11}H_{12}O_2$: C, 74.98; H, 6.86. Found: C, 74.82; H, 6.65.

3,3'-(Bicyclo[1.1.1]pentane-1,3-diyl)dipropiolaldehyde (**20**). To a solution/suspension of **19** (790 mg, 4.483 mmol) in dry CH_2Cl_2 (40 mL) was added Dess-Martin periodinane (DMP, 4.754 g, 11.208 mmol, 2.5 equiv.) at room temperature. The solution turned yellow immediately and the reaction mixture was stirred for 2 h. The suspension dissolved, leaving a clear yellowish solution. Subsequently, solutions of saturated aqueous $Na_2S_2O_3$ (20 mL) and $NaHCO_3$ (20 mL) were added and the mixture was stirred for additional 15 min. The reaction mixture was then diluted with CH_2Cl_2 (100 mL), aqueous phase was removed, the clear yellowish organic phase was washed with a saturated aqueous solution of $Na_2S_2O_3$ and $NaHCO_3$ in 1:1 ratio (2 × 40 mL), and finally dried over $MgSO_4$. The solvent was removed under reduced pressure and a solid yellow residue was sorbed on silica gel (4 g). Column

chromatography on silica gel (CH_2Cl_2) afforded **20** as a white crystalline solid with a distinctive mushroom-like odor (566 mg, 3.287 mmol, 73%).

Mp 147.2 - 148.5 °C. ^{1}H NMR (400 MHz, $CDCl_3$): δ 2.50 (s, 6H), 9.15 (s, 2H). ^{13}C {^{1}H} NMR (100 MHz, $CDCl_3$): δ 30.2, 58.6, 79.8, 93.2, 176.4. IR (KBr): 3006, 2975, 2921, 2885, 2245, 2204, 2150, 1656, 1505, 1451, 1391, 1250, 1164, 1124, 966, 910, 675 cm^{-1}. MS (CI), *m/z* (%): 173.1 (18, M + H), 143.1 (15, M - CHO), 115.1 (100, M - 2CHO), 91.1 (48, M - CHO + CCCHO). HRMS (CI) (*m/z*): $[M + H]^+$ Calcd for $C_{11}H_9O_2^+$, 173.0603; found, 173.0605. Anal. Calcd. for $C_{11}H_8O_2$: C, 76.73; H, 4.68. Found: C, 76.41; H, 4.77.

1,3-Bis(4,4-dibromobut-3-en-1-ynyl)bicyclo[1.1.1]pentane (**21**). A flame-dried and argon filled Schlenk flask was charged with PPh_3 (4.951 g, 18.876 mmol, 6.5 equiv.) and CBr_4 (2.889 g, 8.712 mmol, 3.0 equiv.). After three successive vacuum/argon cycles, the mixture was cooled to 0 °C using an ice bath, dry and degassed CH_2Cl_2 was added (30 mL), and the orange reaction mixture was stirred 30 min at 0 °C and finally 30 min at room temperature. The solution was cooled back to 0 °C and a solution of **20** (500 mg, 2.904 mmol) in dry CH_2Cl_2 (10 mL) was added dropwise. The reaction mixture turned brown immediately. Cooling was stopped and the brown solution was stirred for additional 30 min at room temperature. Silica gel (5 g) was added directly to the reaction mixture and all volatiles were removed under reduced pressure. Column chromatography on silica gel (hexane/CH_2Cl_2 - 1:1) yielded **21** as a white crystalline solid (1.208 g, 2.497 mmol, 86%).

Mp 115.0 - 116.4 °C. ^{1}H NMR (400 MHz, $CDCl_3$): δ 2.41 (s, 6H), 6.52 (s, 2H). ^{13}C {^{1}H} NMR (100 MHz, $CDCl_3$): δ 31.0, 58.7, 77.1, 96.1, 102.0, 119.2. IR (KBr): 3019, 2992, 2965, 2912, 2875, 2226, 2201, 1637, 1576, 1445, 1272, 1254, 1180, 953, 932, 920, 829, 820, 692, 590, 525 cm^{-1}. MS (APCI), *m/z* (%): 484.7 (10, most intense ion of isotope cluster, M + H), 279.1 (100). HRMS (APCI) (*m/z*): $[M + H]^+$ Calcd for $C_{13}H_9Br_4^+$, 480.7432; found, 480.7431. Anal. Calcd. for $C_{13}H_8Br_4$: C, 32.27; H, 1.67. Found: C, 32.33; H, 1.79.

ASSOCIATED CONTENT

Supporting Information. The Supporting Information is available free of charge on the ACS Publications website.

Copies of ^{1}H, ^{13}C NMR spectra of all new compounds, optimized model of **1**@TPP-h_{12}, optimized geometry of **1**, and an ORTEP view of a single molecule and packing in **1**, **2**, **9**, **18**, **19**, and **21** (PDF).
X-ray crystallographic data for compound **1** (CIF)
X-ray crystallographic data for compound **2** (CIF)
X-ray crystallographic data for compound **9** (CIF)
X-ray crystallographic data for compound **18** (CIF)
X-ray crystallographic data for compound **19** (CIF)
X-ray crystallographic data for compound **21** (CIF)
Optimized model of **1**@TPP-h_{12} (PDB)

AUTHOR INFORMATION

Corresponding Author
* kaleta@uochb.cas.cz, wen@uochb.cas.cz
ORCID
J. Kaleta: 0000-0002-5561-7580
G. Bastien: 0000-0001-6374-8620
J. Wen: 0000-0001-6136-8771

M. Dračínský: 0000-0002-4707-8230
I. Císařová: 0000-0002-9612-9831
P. D. Beale: 0000-0001-8452-6891
C. T. Rogers: 0000-0002-2278-6863
J. Michl: 0000-0002-4707-8230

Notes

The authors declare no competing financial interest.

ACKNOWLEDGEMENTS

This work was supported by the Institute of Organic Chemistry and Biochemistry, Academy of Sciences of the Czech Republic (RVO: 61388963) and the US National Science Foundation (DMR-1608424 and DMR-1409981). We thank Dr. Lucie Bednárová for help with IR spectra, Dr. Radek Pohl for help with NMR spectra, and Dr. Monika Benkovičová for acquiring TEM images.

REFERENCES

1. Kottas, G. S.; Clarke, L. I.; Horinek D.; Michl, J. Artificial Molecular Rotors. *Chem. Rev*. **2005**, *105*, 1281.

2. *From Non-Covalent Assemblies to Molecular Machines*; Sauvage, J. P., Gaspard, P., Eds; Wiley-VCH: Weinheim, 2010.

3. *Molecular Devices and Machines: Concepts and Perspectives for the Nanoworld*; Balzani, V., Credi, A., Venturi, M., Eds.; Wiley-VCH: Weinheim, 2008.

4. Erbas-Cakmak, S.; Leigh, D. A.; McTernan, C. T.; Nussbaumer, A. L. Artificial Molecular Machines. *Chem. Rev.* **2015**, *115*, 10081.

5. Catalano, L.; Perez-Estrada, S.; Wang, H.-H.; Ayitou, A. J.-L.; Khan, S. I.; Terraneo, G.; Metrangolo, P.; Brown, S.; Garcia-Garibay, M. A. Rotational Dynamics of Diazabicyclo[2.2.2]octane in Isomorphous Halogen-Bonded Co-crystals: Entropic and Enthalpic Effects. *J. Am. Chem. Soc.* **2017**, *139*, 843-848.

6. Zhao, K.; Dron, P. I.; Kaleta, J.; Rogers, C. T.; Michl, J. Arrays of Dipolar Molecular Rotors in Tris(*o*-phenylenedioxy)cyclotriphosphazene. *Top. Curr. Chem.* **2014**, *354*, 163.

7. van Leeuwen, T.; Lubbe, A. S.; Štacko, P.; Wezenberg, S. J.; Feringa, B. L. Opinion: Studies on the Origin of Life - The End of the Beginning. *Nat. Rev. Chem.* **2017**, *1*, 1-7.

8. Kaleta, J.; Kaletová, E.; Císařová, I.; Teat, S. J.; Michl, J. Synthesis of Triptycene-Based Molecular Rotors for Langmuir-Blodgett Monolayers. *J. Org. Chem.* **2015**, *80*, 10134-10150.

9. Kaleta, J.; Wen, J.; Magnera, T. F.; Dron, P. I.; Chenhui, Z.; Michl, J. Structure of a Monolayer of Molecular Rotors on Aqueous Subphase From Grazing-Incidence X-ray Diffraction. *PNAS* **2018**, *115*, 9373-9378.

10. Cheng, J.; Štacko, P.; Rudolf, P.; Gengler, R. Y. N.; Feringa, B. L. Bidirectional Photomodulation of Surface Tension in Langmuir Films. *Angew. Chem. Int. Ed.* **2016**, *55*, 1-7.

11. Hammerich, M.; Herges, R. Laterally Mounted Azobenzenes on Platforms. *J. Org. Chem.* **2015**, *80*, 11233-11236.

12. Wang, Z.; Heinke, L.; Jelic, J.; Cakici, M.; Dommaschk, M.; Maurer, R. J.; Obenhofer, H.; Grosjean, S.; Herges. R.; Braese, S.; Reuter, K.; Woell, C. Photoswitching in Nanoporous, Crystalline Solids: An Experimental and Theoretical Study for Azobenzene Linkers Incorporated in MOFs. *Phys. Chem. Chem. Phys.* **2015**, *17*, 14582-14587.

13. Otte, F.; Lemke, S.; Schuett, C.; Krekiehn, N. R.; Jung. U.; Magnussen, O. M.; Herges, R. Ordered Monolayers of Free-Standing Porphyrins on Gold. *J. Am. Chem. Soc.* **2014**, *136*, 11248-11251.

14. Chen, K.-Y.; Ivashenko, O.; Carroll, G. T.; Robertus, J.; Kistemaker, J. C. M.; London, G.; Browne, W. R.; Rudolf, P.; Feringa, B. Control of Surface Wettability Using Tripodal Light-Activated Molecular Motors. *J. Am. Chem. Soc.* **2014**, *136*, 3219-3224.

15. Horinek, D.; Michl, J. Surface-Mounted Altitudinal Molecular Rotors in Alternating Electric Field: Single-Molecule Parametric Oscillator Molecular Dynamics. *PNAS* **2005**, *102*, 14175-14180.

16. Pijper, T.; Ivashenko, O.; Walko, M.; Rudolf, P.; Browne, W.; Feringa, B. L. Positron and Orientation Control of a Photo- and Electrochromic Dithienylethene Using a Tripodal Anchor on Gold Surfaces. *J. Phys. Chem. C* **2015**, *119*, 3648-3657.

17. Kobr, L.; Zhao, K.; Shen, Y.; Comotti, A.; Bracco, S.; Shoemaker, R. K.; Sozzani, P.; Clark, N. A.; Price, J. C.; Rogers, C. T.; Michl, J. Inclusion Compound Based Approach to Arrays of Artificial Dipolar Molecular Rotors. A Surface Inclusion. *J. Am. Chem. Soc.* **2012**, *134*, 10122.

18. Kaleta, J.; Dron, P. I.; Zhao, K.; Shen, Y.; Císařová, I.; Rogers, C. T.; Michl, J. Arrays of Molecular Rotors with Triptycene Stoppers: Surface Inclusion in Hexagonal Tris(*o*-phenylenedioxy)cyclotriphosphazene. *J. Org. Chem.* **2015**, *80*, 6173-6192.

19. Kaleta, J.; Chen, J.; Bastien, G.; Dračínský, M.; Mašát, M.; Rogers, C. T.; Feringa, B. L.; Michl, J. Surface Inclusion of Unidirectional Molecular Motors in Hexagonal Tris(*o*-phenylene)cyclotriphosphazene. *J. Am. Chem. Soc.* **2017**, *139*, 10486-10498.

20. Jiang, X.; Duan, H.-B.; Khan, S. I.; Garcia-Garibay, M. A. Diffusion-Controlled Rotation of Triptycene in a Metal–Organic Framework (MOF) Sheds Light on the Viscosity of MOF-Confined Solvent. *ACS Central Science* **2016**, *2*, 608-613.

21. Jiang, X.; O´Brien, Z. J.; Yang, S.; Lai, L. H.; Buenaflor, J.; Tan, C.; Khan, S.; Houk, K. N.; Garcia-Garibay, M. A. Crystal Fluidity Reflected by Fast Rotational Motion at the Core, Branches, and Peripheral Aromatic Groups of a Dendrimeric Molecular Rotor. *J. Am. Chem. Soc.* **2016**, *138*, 4650-4656.

22. Catalano, L.; Perez-Estrada, S.; Terraneo, G.; Pilati, T.; Resnati, G.; Metrangolo, P.; Garcia-Garibay, M. A. Dynamic Characterization of Crystalline Supramolecular Rotors Assembled through Halogen Bonding. *J. Am. Chem. Soc.* **2015**, *137*, 15386-15389.

23. Lemouchi, C.; Iliopoulos, K.; Zorina, L.; Simonov, S.; Wzietek, P.; Cauchy, T.; Fortea, A.; Canadell, E.; Kaleta, J.; Michl, J.; Gindre, D.; Chrysos, M.; Batail, P. Crystalline Arrays of Pairs of Molecular Rotors: Correlated Motion, Rotational Barriers, and Space-Inversion Symmetry Breaking Due to Conformational Mutations. *J. Am. Chem. Soc.* **2013**, *135*, 9366.

24. Lemouchi, C.; Meziere, C.; Zorina, L.; Simonov. S.; Rodriguez-Fortea, A.; Canadell, E.; Wzietek, P.; Auban-Senzier, P.; Pasquier, C.; Giamarchi, T.; Garcia-Garibay, M. A.; Batail, P. Design and Evaluation of a Crystalline Hybrid of Molecular Conductors and Molecular Rotors. *J. Am. Chem. Soc.* **2012**, *134*, 7880-7891.

25. Setaka, W.; Yamaguchi, K. Order-Disorder Transition of Dipolar Rotor in a Crystalline Molecular Gyrotop and Its Optical Change. *J. Am. Chem. Soc.* **2013**, *135*, 14560-14563.

26. Rodríguez-Fortea, A.; Kaleta, J.; Mézièbre, C.; Allain, M.; Canadell, E.; Wzietek, P.; Michl, J.; Batail, P. Asymmetric Choreography in Pairs of Orthogonal Rotors. *ACS Omega* **2018**, *3*, 1293-1297.

27. Cipolloni, M.; Kaleta, J.; Mašát, M.; Dron, P. I.; Shen, Y.; Zhao, K.; Rogers, C. T.; Shoemaker, R. K.; Michl, J. Time-Resolved Fluorescence Anisotropy of Bicyclo[1.1.1]pentane/Tolane-Based Molecular Rods Included in Tris(*o*-phenylenedioxy)cyclotriphosphazene (TPP). *J. Phys. Chem. C* **2015**, *119*, 8805-8820.

28. Dron, P. I.; Zhao, K.; Kaleta, J.; Shen, Y.; Wen, J.; Shoemaker, R. K.; Rogers, C. T.; Michl, J. Bulk Inclusions of Pyridazine Based Molecular Rotors in Tris(*o*-phenylenedioxy)cyclotriphosphazene (TPP). *Adv. Funct. Mater.* **2016**, *26*, 5718-5732.

29. Kobr, L.; Zhao, K.; Shen, Y.; Shoemake, R. K.; Rogers, C. T.; Michl, J. Tris(*o*-phenylenedioxy)cyclotriphosphazene (TPP) Inclusion Compounds Containing a Dipolar Molecular Rotor. *Cryst. Growth Des.* **2014**, *14*, 559-568.

30. Allcock, H. R.; Allen, R. W.; Bissell, E. C.; Smeltz, L. A.; Teeter, M. Phosphorus-Nitrogen Compounds. 26. Molecular Motion and Molecular Separations in Cyclophosphazene Clathrates. *J. Am. Chem. Soc.* **1976**, *98*, 5120.

31. Sozzani, P.; Bracco, S.; Comotti, A.; Ferretti, L.; Simonutti, R. Methane and Karbon Dioxide Storage in a Porous van der Waals Crystal. *Angew. Chem.* **2005**, *117*, 1850.

32. Rozenbaum, V. M.; Ogenko, V. M.; Chuiko, A. A. Vibrational and Orientational States of Surface Atomic Groups. *Phys.-Usp.* **1991**, *34*, 883.

33. Li, H.; Franks, K. J.; Hanson, R. J.; Kong, W. Brute Force Orientation and Alignment of Pyridazine Probed by Resonantly Enhanced Multiphoton Ionization. *J. Phys. Chem. A* **1998**, *102*, 8084.

34. Rezác, J.; Hobza, P. Advanced Corrections of Hydrogen Bonding and Dispersion for Semiempirical Quantum Mechanical Methods. *J. Chem. Theory Comput.* **2012**, *8*, 141-151.

35. Grimme, S.; Ehrlich, S.; Goerigk, L. Effect of the Damping Function in Dispersion Corrected Density Functional Theory. *J. Comp. Chem.* **2011**, *32*, 1456-1465.

36. Coates, W. J.; McKillop, A. One-Pot Preparation of 6-Substituted 3-(2*H*)-Pyridazinones from Ketones. *Synthesis*, **1993**, *3*, 334-342.

37. Kaleta, J.; Mazal, C. Triangular Macrocycle Altering Planar and Bulky Sections in Its Molecular Backbone. *Org. Lett.* **2011**, *13*, 1326-1329.

38. Kaleta, J.; Nečas, M.; Mazal, C. 1,3-Diethynylbicyclo[1.1.1]pentane, a Useful Molecular Building Block. *Eur. J. Org. Chem.* **2012**, *25*, 4783-4796.

39. Alemany, L. B.; Grant, D. M.; Pugmire, R. J.; Alger, T. D.; Zilm, K. W. Cross Polarization and Magic Angle Sample Spinning NMR Spectra of Model Organic Compounds. 2. Molecules of Low or Remote Protonation. *J. Am. Chem. Soc.* **1983**, *105*, 2142-2147.

40. Paluch, P.; Pawlak, T.; Jezioma, A.; Trébosc, J.; Hou, G.; Vega, A. J.; Amoureux, J.-P.; Dračínský, M.; Polenova, M.; Potrzebowski, M. J. Analysis of Local Molecular Motions of Aromatic Sidechains in Proteins by 2D and 3D Fast MAS NMR Spectroscopy and Quantum Mechanical Calculations. *Phys. Chem. Chem. Phys.* **2015**, *17*, 28789-28801.

41. Gall, C. M.; Cross, T. A.; Diverdi, J. A.; Opella, S. J. Protein Dynamics by Solid-State NMR: Aromatic Rings of the Coat Protein in Bacteriophage. *PNAS* **1982**, *79*, 101-105.

42. Comotti, A.; Simonutti, R.; Stramera, S.; Sozzani, P. ^{13}C and ^{31}P MAS NMR Investigations of Spirocyclotriphosphazene Nanotubes. *Nanotechnology* **1999**, *10*, 70.

43. Comotti, A.; Bracco, S.; Ferretti, L.; Mauri, M.; Simonutti, R.; Sozzani, P. A Single-Crystal Imprints Macroscopic Orientation on Xenon Atoms. *Chem. Commun.* **2007**, 350.

44. MOPAC2016, Version: 17.119L, James J. P. Stewart, Stewart Computational Chemistry, web: HTTP://OpenMOPAC.net.

45. Kaleta, J.; Janoušek, Z.; Nečas, M.; Mazal, C. Molecular Rods Combining *o*-Carborane and Bicyclo[1.1.1]pentane Cages: An Insertion of the Triple Bond Located Next to a Highly Strained Cage. *Organometallics* **2015**, *34*, 967-972.

46. Kaleta, J.; Michl, J.; Mézièrе, C.; Simonov, S.; Zorina, L.; Wzietek, P.; Rodríguez-Fortea, A.; Canadell, E.; Batail, P. Gearing Motion in Cogwheel Pairs of Molecular Rotors: Weak-Coupling Limit. *CrystEngComm* **2015**, *17*, 7829-7834.

47. Kaleta, J.; Michl, J., Mazal, C. T-Shaped Molecular Building Blocks by Combined Bridgehead and Bridge Substitution on Bicyclo[1.1.1]pentanes. *J. Org. Chem.* **2010**, *75*, 2350-2356.

48. Schwab, P. F. H.; Noll, B. C.; Michl, J. Synthesis and Structure of Trigonal and Tetragonal Connectors for a "Tinkertoy" Construction Set. *J. Org. Chem.* **2002**, *67*, 5476-5485.

49. Kaleta, J.; Bastien, G.; Císařová, I.; Batail, P.; Michl, J. Molecular Rods: Facile Desymmetrization of 1,4-Diethynylbicyclo[2.2.2]octane. *Eur. J. Org. Chem.* **2018**, *37*, 5137-5142.

50. Allcock, H. R.; Levin, M. L.; Whittle, R. R. Tris(*o*-phenylenedioxy)cyclotriphosphazene: The Clathration-Induced Monoclinic to Hexagonal Solid-State Transition. *Inorg. Chem.* **1986**, *25,* 41-47.

51. Sozzani, P.; Comotti, A.; Simonutti, R.; Meersamnn, T.; Logan, J. W.; Pines, A. A Porous Crystalline Molecular Solid Explored by Hyperpolarized Xenon. *Angew. Chem. Int. Ed.* **2000**, *39*, 2695; *Angew. Chem.* **2000**, *112*, 2807.

52. Sozzani, P.; Bracco, S.; Comotti, A.; Ferretti, L.; Simonutti, R. Methane and Carbon Dioxide Storage in a Porous van der Waals Crystal. *Angew. Chem. Int. Ed.* **2005**, *44*, 1816.

53. Hoffman, J. D. Hindered Intermolecular Rotation in the Solid State: Thermal and Dielectric Phenomena in Long Chain Compounds. *J. Chem. Phys.* **1952**, *20*, 541.

54. Hoffman, J. D.; Pfeiffer, H. G. Theory of Dielectric Relaxation for a Single Axis Rotator in a Crystalline Field. *J. Chem. Phys.* **1954**, *22*, 132.

55. Hoffman, J. D. Theory of Dielectric Relaxation for a Single Axis Rotator in a Crystalline Field. II. *J. Chem. Phys.* **1955**, *23*, 1331.

56. P. Debye, *Polar Molecules,* Dover Publications, New York, 1945.

57. H. Frohlich, *Theory of Dielectrics,* Oxford University Press, London, England, 1949.

58. Sheldrick, G.M. SHELXT - Integrated Space-Group and Crystal-Structure Determination. *Acta Cryst.* **2015**, *A71*, 3-8.

59. Sheldrick, G.M. Crystal Structure Refinement with SHELXL. *Acta Cryst.* **2015**, *C71*, 3-8.

60. Stewart J. J. Optimization of Parameters for Semiempirical Methods VI: More Modifications to the NDDO Approximations and Re-Optimization of Parameters. *J. Mol. Model.* **2013**, 19, 1-32.

61. MOPAC2016, Version: 17.119L, James J. P. Stewart, Stewart Computational Chemistry, web: HTTP://OpenMOPAC.net.

62. TURBOMOLE V7.2 2017, a development of University of Karlsruhe and Forschungszentrum Karlsruhe GmbH, 1989-2007, TURBOMOLE GmbH, since 2007; available from http://www.turbomole.com.

63. Clark, S. J.; Segall, M. D.; Pickard, C. J.; Hasnip, P. J.; Probert, M. J.; Refson, K.; Payne, M. C. First Principles Methods Using CASTEP. *Z. Kristallogr.* **2005**, *220*, 567-570.

64. Perdew, J. P.; Burke, K.; Ernzerhof, M. Generalized Gradient Approximation Made Simple. *Phys. Rev. Lett.* **1996**, *77*, 3865-3868.

65. Monkhorst, H. J.; Pack, J. D., Special Points for Brillouin-Zone Integrations. *Phys. Rev. B* **1976**, *13*, 5188-5192.

66. Pickard, C. J.; Mauri, F., All-Electron Magnetic Response with Pseudopotentials: NMR Chemical Shifts. *Phys. Rev. B* **2001**, *6324*, 245101.

67. Yates, J. R.; Pickard, C. J.; Mauri, F. Calculation of NMR Chemical Shifts for Extended Systems Using Ultrasoft Pseudopotentials. *Phys. Rev. B* **2007**, *76*, 024401.